Correspondence to:
S. Schröder,
stefanus.schroeder@dlr.de

The Boulder Population of Asteroid 4 Vesta: Size-Frequency Distribution and Survival Time

Stefan E. Schröder[1] , Uri Carsenty[1] , Ernst Hauber[1] , Franziska Schulzeck[1], Carol A. Raymond[2] , and Christopher T. Russell[3]

[1]Deutsches Zentrum für Luft- und Raumfahrt (DLR), Berlin, Germany, [2]Jet Propulsion Laboratory (JPL), California Institute of Technology, Pasadena, CA, USA, [3]Institute of Geophysics and Planetary Physics (IGPP), University of California, Los Angeles, CA, USA

Abstract   Dawn's framing camera observed boulders on the surface of Vesta when the spacecraft was in its lowest orbit (Low Altitude Mapping Orbit, LAMO). We identified, measured, and mapped boulders in LAMO images, which have a scale of 20 m per pixel. We estimate that our sample is virtually complete down to a boulder size of 4 pixels (80 m). The largest boulder is a 400 m-sized block on the Marcia crater floor. Relatively few boulders reside in a large area of relatively low albedo, surmised to be the carbon-rich ejecta of the Veneneia basin, either because boulders form less easily here or live shorter. By comparing the density of boulders around craters with a known age, we find that the maximum boulder lifetime is about 300 Ma. The boulder size-frequency distribution (SFD) is generally assumed to follow a power law. We fit power laws to the Vesta SFD by means of the maximum likelihood method, but they do not fit well. Our analysis of power law exponents for boulders on other small Solar System bodies suggests that the derived exponent is primarily a function of boulder size range. The Weibull distribution mimics this behavior and fits the Vesta boulder SFD well. The Weibull distribution is often encountered in rock grinding experiments and may result from the fractal nature of cracks propagating in the rock interior. We propose that, in general, the SFD of particles (including boulders) on the surface of small bodies follows a Weibull distribution rather than a power law.
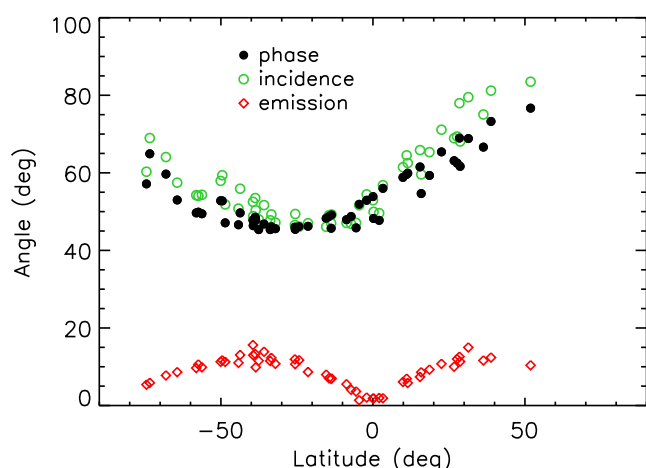
1. Introduction

Boulders on small Solar System bodies provide a window into the interior. Boulders may be created by spallation during large impacts and therefore are typically found in and around fresh craters. They do not survive forever but are gradually eroded into dust by exposure to the space environment (Basilevsky et al., 2015; Delbo et al., 2014). In the literature, the location and outline of boulders are typically mapped, and a size-frequency distribution (SFD) is produced. Studies of main-belt asteroids often focus on finding the crater of origin of sparsely distributed boulders (Küppers et al., 2012; Lee et al., 1996; Thomas et al., 2001). In contrast, the surface of near-Earth asteroids is densely populated by boulders of all sizes, all thought to originate from the destruction of a parent body (DellaGiustina et al., 2019; Mazrouei et al., 2014; Michikami et al., 2019). Generally, a power law is fitted to the cumulative boulder SFD, with an exponent defining the slope. In a seminal paper, Hartmann (1969) provided a table in which empirically derived exponents are linked to various geological processes. The largest exponent in the table is associated with the ejecta of hypervelocity impacts. The exponents of asteroid boulder SFDs are generally found to be close to this value. However, published exponents show considerable variation, and the reason for this is often not clear. What clues does a particular value of the exponent provide to the composition and physical properties of the surface?

From its vantage point in the lowest mapping orbit, the NASA Dawn spacecraft was able to distinguish boulders on the surface of Vesta. A first analysis of the global boulder population was performed by Denevi et al. (2016), who inferred a typical regolith depth of about 1 km. We extend their analysis by mapping the location of all boulders that we could recognize to investigate their distribution in and around individual craters, as well as the distribution of craters with boulders over the surface. We estimate the average boulder lifetime by comparing the boulder density around craters for which an age estimate is available (Kneissl et al., 2014; Ruesch et al., 2014; Schmedemann et al., 2014) and assess the Basilevsky et al. (2015) prediction that meter-sized boulders on Vesta live roughly 30 times shorter than on the Moon. We also determined

Figure 1. Boulder viewing conditions: photometric angles at the center of selected LAMO images.

the SFD of boulder populations of individual craters and that of the global population. Vesta is a very large asteroid, and on its surface we found boulders with a size of hundreds of meters, larger than those found on other asteroids, with the exception of Ceres (Schulzeck et al., 2018). Such huge objects are also rare on Earth (Bruno & Ruban, 2017), and we will therefore explore a relatively unknown part of the boulder SFD. The official geological term for terrestrial particles larger than a few meters is "megaclast." According to Bruno and Ruban (2017), our Vesta megaclasts classify as megablocks ($10 < d < 100$ m) and superblocks ($d > 100$ m). In this paper we will continue to refer to all Vesta megaclasts as "boulders," for convenience. We compare the Vesta boulder SFD with that of other small bodies. This is made challenging by the fact that different fitting methods have been used in the literature to fit the power law, only one of which, the maximum likelihood (ML) method, is statistically correct (Clauset et al., 2009). We therefore carefully assess published exponents and in some cases reanalyze the original data using the ML method.

In this paper we only discuss boulders on small bodies. We do not discuss boulders on Earth and Mars, which are often formed and weathered by forces other than those imposed by the space environment (tectonic, aeolian, and biological) (Pajola et al., 2017). Neither do we consider boulders on comets, as they are not thought to result from impacts but rather from processes like sublimation, activity outbursts, and the associated uplifting and redeposition (Pajola et al., 2015).
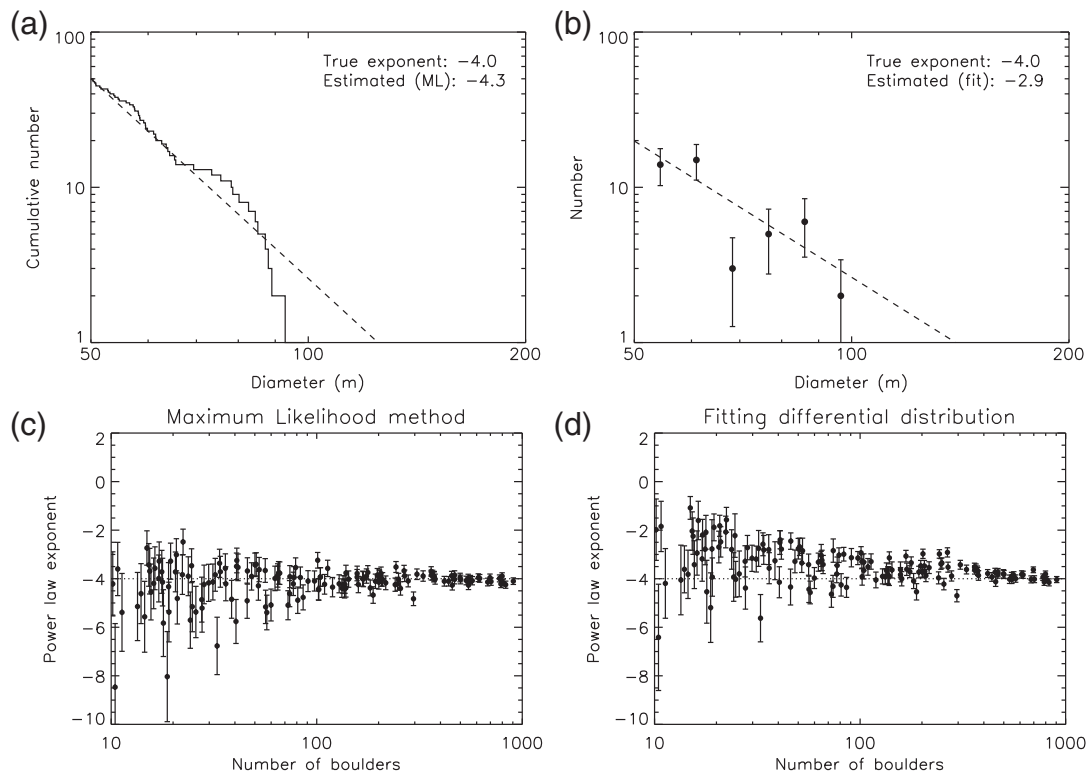
2. Methodology

2.1. Boulder Mapping

Boulders on Vesta can only be distinguished in framing camera images from the Low Altitude Mapping Orbit (LAMO), which were acquired between 13 December 2011 and 30 April 2012 at an altitude of 180 km (Russell et al., 2007). The framing camera is a narrow-angle camera with a field of view of $5.5° \times 5.5°$ (Sierks et al., 2011). LAMO images have the highest resolution of all images acquired at Vesta. Most LAMO images have a spatial resolution between 17 and 22 m, although south of latitude −45° the resolution is a little lower (Roatsch et al., 2013). When we talk about "pixels" in this paper, we always refer to LAMO pixels. We selected 53 LAMO images that we used in our analysis (at least one for each crater with boulders) and determined their average spatial resolution as 20 ± 2 m per pixel. In this paper, we therefore adopt a typical LAMO image resolution of 20 m per pixel. We are confident that we could reliably identify a boulder for a size of at least 3 pixels (60 m) using the method described below, although we mapped suspected boulders smaller than that. However, we cannot assume our count is complete with the 3 pixels criterion, if only because of the measurement uncertainty. A criterion of 4 pixels (80 m) is more likely to ensure near completeness (Pajola et al., 2016). The photometric angles at the center of the 53 images are plotted as a function of latitude in Figure 1. The illumination and observation conditions during LAMO were relatively constant. The average photometric angles at the center of the images are incidence $\iota = 57° \pm 10°$, emission $\epsilon = 9° \pm 4°$, and phase $\alpha = 54° \pm 8°$. The incidence and phase angles become relatively large only toward the midlatitudes in the northern hemisphere (+50°), which were partly in the shadow. This means that the majority of boulders were observed under similar conditions.

The second author reviewed the entire LAMO data set and identified, measured, and mapped all boulders using the J-Vesta GIS program, which is a version of JMARS (https://jmars.mars.asu.edu/) (Christensen et al., 2009). The first author reviewed these results for accuracy and completeness. Despite our best efforts, systematic errors may result from mapping being performed by a single individual. Such bias may be avoided by the use of automated boulder detection algorithms, such as one recently developed for crater counting purposes (Benedix et al., 2020). The location of boulders (and craters) is defined in the Claudia coordinate system (Russell et al., 2012). Boulders were identified as positive relief features in projected images at a zoom level of 1,024 pixels per degree. The native LAMO resolution is ∼200 pixels per degree, so this represents a zoom factor of about 5. The boulder size was determined using the J-Vesta crater measuring tool, which draws a circle around the boulder fitted to 3 points that are selected by the user on the visible boulder outline. The vast majority of boulders that we mapped were too small to clearly distinguish the shape,

Figure 2. Monte Carlo simulations of boulder populations, generated assuming the cumulative SFD follows a power law with exponent −4. (a and b) A population of 50 boulders with a minimum size of 50 m, shown as (a) a cumulative plot with the power law exponent estimated by the ML method and (b) a binned, differential plot with the exponent estimated by a least squares fit. The dashed lines are the best fit power laws. (c and d) Estimating the power law exponents of 150 boulder populations by (c) ML and (d) fitting the differential distribution. The populations were randomly generated in the logarithmic interval (10, 1,000) for the number of boulders. The dotted line indicates the exponent's true value.

and we therefore chose the circle as a reasonable approximation. The first author also mapped boulders for a single crater using the same method to confirm that the measurement uncertainty is about a single pixel. While mapping, there were several challenges to overcome. The limited accuracy of pointing information for LAMO images leads to mismatches between projected images. We used small craters inside and outside the crater as tie points to align the projected images to the Vesta background mosaic and to align images relative to each other. J-Vesta allows shifting the projected image relative to the background in the horizontal and the vertical direction, but rotation is not possible. All this leads to uncertainty in the location of boulders on the order of 500 m. In addition, unusually bright inner walls of fresh craters could appear saturated, making it impossible to recognize any feature on their surface, due to a limitation in J-Vesta with image brightness scaling. Generally, on crater walls it was difficult to distinguish genuine boulders from rocky outcrops, which are prevalent just below the rim. When in doubt, we did not include such features in our sample. It was also difficult to decide whether a large mound was a degraded boulder or had always been simply a pile of rubble. The north pole of Vesta was in the shadow at the time of LAMO (December 2011 to April 2012). Therefore, counts of boulders around craters are incomplete north of latitude +30°, and it was not possible to identify boulders north of +60°.

2.2. Size-Frequency Distribution

Boulder SFDs are often displayed in cumulative format, following the recommendation by the Crater Analysis Techniques Working Group (1979) for crater SFDs to be plotted in both the cumulative and differential format. For the latter, the Working Group recommended a relative distribution known as the R-plot. In this paper, we display the boulder SFD in both cumulative and differential format but choose the incremental (binned, histogram) version for the latter (Colwell, 1993). Figure 2 illustrates both formats for a simulated boulder population.

The cumulative format has become especially popular in the literature (perhaps because of its remarkable ability to convert even the noisiest data into a smooth downward curve), and figures in differential format are

often omitted from boulder (and crater) counting papers. Several unfortunate practices associated with the cumulative distribution have become established in the literature. The first is binning. The Crater Analysis Techniques Working Group (1979) wrote that the "collection, manipulation, and display of unbinned data is more time consuming than for binned data." This may have been true in 1979 but is no longer the case. Binning of a cumulative distribution is not merely unnecessary but represents a loss of information. Also, bins that have the same value as their neighbor on the right are often not displayed. Their omission skews the appearance of the distribution and affects how we perceive the goodness of fit of a model curve. Another statistically suspect practice is the association of Poisson (square root) error bars with the bins. Such error bars are valid for single bins when considered in isolation, but in a plot of the cumulative distribution they do not serve their usual purpose of indicating the uncertainty of the data: Regardless of the size of its bar, the number in a bin can neither be lower than its neighbor on the right nor higher than its neighbor on the left. Therefore, we do not bin the cumulative distribution in this paper. The differential distribution is always binned in practice, where the bin width can be chosen as constant on a linear or logarithmic scale. Poisson error bars associated with the bins are statistically meaningful and will give the correct impression of how well the data agree with a particular model curve. Empty bins, however, present a problem. SFD plots are invariably shown on a log-log scale, and empty bins cannot be displayed, which skews the appearance of the distribution. Moreover, empty bins cannot be included when fitting models (such as a power law) to the logarithm of the data, introducing bias.

2.3. Power Law Fitting

The cumulative distribution of boulders on Solar System bodies is generally assumed to follow a power law. The number of boulders with a size larger than d is

$$N(> d) = N_{\text{tot}} \left(\frac{d}{d_{\min}} \right)^{\alpha}, \tag{1}$$

with $\alpha < 0$ the power law exponent and N_{tot} the total number of boulders larger than $d_{\min}$. Hartmann (1969) showed that the exponent of a cumulative distribution of a quantity that follows a power law is identical to that of the associated incremental differential distribution with a constant bin size on a logarithmic scale. Colwell (1993) added that this is only true if the logarithmic bins are chosen wide enough. If the bin size of the incremental differential distribution is constant on a linear scale, then the exponent differs by unity from that of the cumulative distribution. Historically, the power law exponent was estimated by fitting a line to the cumulative distribution plotted on a log-log scale, either by eye or by means of a least squares algorithm. There are two problems associated with this practice. First, the differential distribution may clearly show that a certain quantity does not follow a power law, but the associated cumulative distribution may still give the impression that it does. Second, the uncertainty of the power law exponent cannot be reliably retrieved by means of simple linear regression because of the ill-defined errors associated with the cumulative bins. Uncertainties given for exponents derived from a conventional fit to the cumulative distribution are underestimated (Clauset et al., 2009). A statistically sound way to estimate the power law exponent from the SFD is the ML method (Clauset et al., 2009; Newman, 2005). In the ML method, the power law exponent is calculated directly from the boulder size measurements and is therefore independent of how the data are displayed (cumulative, differential, and binning). The ML estimate for the power law exponent ($\alpha < 0$) is

$$\hat{\alpha} = -N \left(\sum_{i=1}^{N} \ln \frac{d_i}{d_{\min}} \right)^{-1}, \tag{2}$$

with d_i the size of boulder i and N the total number of boulders with a size larger than $d_{\min}$. The standard error of $\hat{\alpha}$ is

$$\sigma = -\hat{\alpha}/\sqrt{N} \tag{3}$$

plus higher-order terms, which we ignore in this paper. We note that the cumulative power law exponent alpha ($\alpha_S < 0$) in Equation 2 relates to the scaling parameter alpha ($\alpha_C > 0$) in Clauset et al. (2009) as $\alpha_S = 1 - \alpha_C$. The estimator in Equation 2 is unbiased only for sufficiently large sample size; Clauset et al. (2009) suggest $N > 50$. Clauset et al. (2009) also provide details to a statistical test that evaluates whether a power law is an appropriate model for the data. The test randomly generates a large number of synthetic data sets according to the best fit power law model (specified by $\hat{\alpha}$ and $d_{\min}$) and calculates for each the so-called

Kolmogorov-Smirnov statistic, which is a measure of how well the synthetic data agree with the model. A p value, defined as the fraction of synthetic data sets that have a larger statistic than the real data set, quantifies how well the power law performs. The authors adopt $p < 0.1$ to mean rejection of the power law model.

An example of a fit with the ML method is shown in Figure 2a. In this paper, we generally display the power law associated with a ML-derived exponent in plots of both the cumulative and differential distributions. Displaying it in the latter format requires an additional step of performing a conventional fit to the differential distribution to estimate the intercept in addition to the exponent. In case the individual boulder sizes are not available, the ML method cannot be applied. If binned boulder numbers as a function of size are available, fitting a power law to the incremental differential distribution in a log-log plot by means of a least squares algorithm is preferred over fitting a power law to the cumulative distribution. Still, one must choose an appropriate bin size and the necessary exclusion of empty bins (the logarithm of zero is undefined) introduces bias, as we will quantify below. One could resolve the problem of empty bins by fitting the power law to the data on a linear scale, but this gives unduly weight to bins with larger numbers toward smaller boulder sizes, which runs counter to the purpose of the power law (describing identical behavior over a wide range of scales). An example of a power law fit to the differential distribution is shown in Figure 2b.

2.4. Monte Carlo Simulations

To investigate the statistical power of the different methods to retrieve the power law exponent (ML and differential fit) and to uncover any associated bias, we simulate the process by randomly generating power law distributions. Fitting a power law to the cumulative distribution is such poor practice that we do not evaluate the method here. The continuous power law probability distribution is also known as the Pareto distribution (Newman, 2005). To simulate a size distribution of boulders associated with impact craters, we draw a random variate U from a uniform distribution on (0, 1) using the RANDOMU routine in IDL with an undefined seed. Then the boulder diameter

$$d = d_{\min} U^{1/\alpha} \tag{4}$$

follows a Pareto distribution, with α the power law index (associated with the cumulative distribution function, with $\alpha < 0$) and $d_{\min}$ the minimum boulder diameter. We start our investigation by generating 150 boulder populations with the number of boulders in each chosen randomly in the logarithmic interval (10, 1,000). For each population, the number of boulders served as input to Equation 4 to generate a SFD that obeys a power law with a (cumulative) exponent of -4.0. Then we estimate the power law exponent of each simulated population by means of two alternative methods: the ML method and a conventional (least squares) power law fit to the differential distribution in log-log format. The ML method estimates the power law exponent straight from the boulder counts, but when fitting the differential distribution one must make several choices. For practical purposes we adopt the parameters used in this paper to represent Vesta: a minimum boulder size of $d_{\min} = 80$ m and a constant bin width of 0.07 on a logarithmic scale. This corresponds to $\beta = 10^{0.07} - 1 = 0.17$ and meets the bin width criterion of Colwell (1993), so that the derived exponent should be the same as that of the cumulative distribution. We exclude any filled bins beyond the first empty one from the fit, which introduces bias in the estimated exponents, especially for small boulder populations (simply excluding empty bins from the fit introduces a different bias). Fitting was performed using the Levenberg-Marquardt algorithm with constrained search spaces for the model parameters (Markwardt, 2009; Moré, 1978). The Poisson errors on the logarithm of the binned counts are asymmetric, and we pass the logarithm of the upper error to the fitting routine.

The results of the simulation are shown in Figures 2c and 2d. For both methods, a large number of boulders is required to reliably estimate the power law exponent. But even for 1,000 boulders the estimated exponent may differ from the true value (-4.0) by up to 0.3, simply by chance. For 100 boulders the estimate exponent is typically off by unity. Below 100 boulders the estimated exponent may rapidly diverge from the true value. For more than 200 boulders, the two methods give similar results. For smaller numbers, however, the estimated exponents are not distributed symmetrically around the true value. For the ML method this is the bias indicated by Clauset et al. (2009). It appears to be negative, but the situation is more complicated than Figure 2c suggests. The median exponent is actually -4.0, meaning that exponents smaller and larger than -4 are found in roughly equal numbers. However, compared to the true value, the estimated exponent can be much more negative (down to -9) than less negative (up to -2). This is reflected in the mean of the exponents in the figure, which is -4.2. For the method of fitting the differential distribution (Figure 2d) the

median and mean of the exponents are -3.6 and -3.5, respectively. This positive bias results from the afore-mentioned exclusion of empty bins and affects boulder populations of all sizes. Therefore, the differential fit method is less accurate than the ML method.

We find that the derived power law exponent for populations with a small number of boulders is always biased, but more so for the differential fit method than for the ML method. For the latter, we recommend a population size of at least 100 boulders for which the size is accurately known (at least 4 image pixels). Here we are more conservative than Clauset et al. (2009), who recommended a minimum sample size of 50. For larger boulder numbers, the estimated exponent generally differs from the true value by less than unity. But even with 1,000 boulders, we can still expect differences of up to 0.3. This is important to keep in mind, for example, when we consult Hartmann (1969) for the interpretation of the power law exponent. The author provided a list of exponents associated with fragmented rocks created by different geological processes with an accuracy of two decimal numbers. We verified that an accuracy of 0.01 for the exponent is only derived from populations of at least a million fragments of known size.

2.5. Weibull Distribution

Although the power law enjoys widespread use as a model for the boulder SFD, it does not always fit the data well. Several authors used exponential functions to fit the SFD of boulders on Mars (Golombek & Rapp, 1997; Golombek et al., 2003; Pajola et al., 2017), and Pajola et al. (2019) found the Weibull distribution to fit the SFD of boulders around a lunar crater better than a power law. Exponential functions can be considered as variations of the Weibull distribution, so it is worth considering the latter as a viable alternative to the power law.

The Weibull distribution was initially derived empirically and is often used to describe the particle distribution resulting from grinding experiments (Rosin & Rammler, 1933). Seeking to describe such a distribution, Brown (1989) developed a theory of sequential fragmentation. He defined the particle distribution as

$$n(m) = C \int_m^\infty n(m') f(m' \to m) dm', \tag{5}$$

where $n(m)$ is the number of particles per unit mass of mass between m and $m + dm$. The function f describes the mass distribution that results when a single fragment of mass $m' > m$ breaks into smaller, lighter pieces, and takes the form of a power law:

$$f(m' \to m) = \left(\frac{m}{m_1} \right)^\gamma, \tag{6}$$

with exponent $-1 < \gamma < 0$ and m_1 a scaling factor related to the average mass in the distribution $n(m)$. The mass on the right-hand side of Equation 6 is m and not m'. Brown and Wohletz (1995) showed that a power law follows naturally from a single-event fragmentation that leads to a branching tree of cracks that have a fractal character. The spacing of the cracks is described by the fractal dimension $D_f = -3\gamma$. The solution of Equation 5 is a Weibull distribution:

$$n(m) = \frac{N_T}{m_1} \left(\frac{m}{m_1} \right)^\gamma \exp \left[-\frac{(m/m_1)^{\gamma+1}}{\gamma + 1} \right], \tag{7}$$

with Weibull shape parameter $\gamma + 1$. The cumulative form of Equation 7 is given by

$$N(> m) = N_T \exp \left[-\frac{(m/m_1)^{\gamma+1}}{\gamma + 1} \right]. \tag{8}$$

For use in this paper, we convert Equation 8 to an expression for the cumulative number density as a function of particle diameter d:

$$N(> d) = N_T \exp \left[-\frac{(d/d_1)^{3(\gamma+1)}}{\gamma + 1} \right], \tag{9}$$

using $m/m_1 = (d/d_1)^3$, with d_1 a size scaling constant. The Weibull shape parameter in Equation 9 is $3(\gamma + 1)$. In practice, we only include boulders larger than a certain size in the analysis. That means that we are dealing with a left-truncated Weibull distribution with the cumulative form (Wingo, 1989):

$$N(> d) = N \exp \left[-\alpha \left(d_i^\beta - d_{\min}^\beta \right) \right], \tag{10}$$

Table 1
All Craters on Vesta With at Least One Boulder Larger Than 4 Pixels (d > 80 m)

Name	Longitude (°E)	Latitude (°)	D (km)	d_{max} (m)	$n_{d > 3px}$	$n_{d > 4px}$	α	σ_α
Aelia	140.7	−14.2	4.7	94	22	4		
Angioletta	29.3	−40.1	18.6	129	87	14	−6.8	1.8
Antonia	200.9	−58.9	17.3	154	491	187	−5.4	0.4
Aquilia	41.1	−50.0	33.8	250	143	71	−4.0	0.5
Arruntia	71.6	+39.4	10.4	109	60	16	−8.3	2.1
Canuleia	294.5	−33.5	11.2	121	67	11	−5.8	1.8
Charito	300.5	−44.5	6.8	109	43	9	−5.3	1.8
Cornelia	225.5	−9.0	16.7	157	221	60	−5.0	0.6
Drusilla	261.2	−14.8	20.9	136	85	33	−8.5	1.5
Eusebia	204.8	−43.1	23.3	113	133	27	−6.5	1.3
Fabia	265.8	+15.6	11.9	152	259	86	−5.8	0.6
Fausta	309.7	−25.5	3.2	111	17	3		
Fonteia	141.5	−53.5	21.1	166	162	56	−4.3	0.6
Galeria	228.3	−29.5	22.9	170	69	31	−3.4	0.6
Gegania	60.8	+3.9	23.8	269	30	14	−4.0	1.1
Hortensia	15.1	−46.6	29.5	218	34	16	−5.7	1.4
Justina	318.0	−34.0	7.1	193	96	23	−5.1	1.1
Lepida	306.7	+18.3	40.2	146	30	11	−4.7	1.4
Licinia	17.2	+23.6	23.6	216	280	111	−4.1	0.4
Mamilia	291.8	+48.3	35.0	142	38	22	−5.5	1.2
Marcia	190.2	+9.5	61.0	390	958	476	−3.6	0.2
Numisia	247.5	−7.7	30.0	174	136	36	−4.4	0.7
Oppia	308.9	−7.6	34.0	164	65	32	−4.3	0.8
Paculla	1.8	−64.0	19.4	172	177	59	−5.4	0.7
Pinaria	32.0	−29.2	38.0	277	315	143	−4.4	0.4
Portia	41.5	+0.9	10.9	155	17	6	−3.5	1.4
Publicia	84.4	+14.6	16.6	110	28	6	−7.9	3.2
Rubria	18.3	−7.4	10.3	113	97	19	−7.5	1.7
Rufillia	138.7	−13.0	15.5	109	25	7	−6.0	2.3
Scantia	274.6	+29.7	16.4	185	182	86	−4.2	0.5
Serena	120.6	−20.4	19.0	119	16	4		
Severina	122.7	−76.3	33.4	248	182	82	−3.8	0.4
Sextilia	146.1	−39.0	19.8	234	69	25	−4.6	0.9
Sossia	286.0	−37.0	7.4	109	32	5		
Teia	271.0	−3.5	6.5	144	37	10	−4.7	1.5
Tuccia	198.1	−39.7	3.3	97	52	10	−10.2	3.2
Unnamed2	74.0	+27.5	11.7	145	69	25	−4.8	1.0
Unnamed3	211.0	−24.0	11.7	120	97	22	−7.8	1.7
Unnamed4	280.2	+7.9	16.1	165	302	92	−5.5	0.6
Unnamed5	351.0	+17.6	3.9	93	47	8	−15.5	5.5
Unnamed6	348.0	−35.0	7.4	138	31	7	−4.0	1.5
Unnamed7	175.8	+33.2	22.5	104	19	6	−7.5	3.0
Unnamed8	116.0	+32.7	20.5	169	41	17	−5.6	1.4

Table 1 *(continued)*

Name	Longitude (°E)	Latitude (°)	D (km)	d_{max} (m)	$n_{d>3px}$	$n_{d>4px}$	α	σ_α
Unnamed9	297.8	+37.6	10.4	130	16	3		
Unnamed10	358.4	+15.1	10.1	107	66	13	−10.6	2.9
Unnamed11	269.3	−73.1	6.2	97	20	7	−12.8	4.8
Unnamed12	291.8	−73.8	7.5	217	99	32	−4.4	0.8
Unnamed13	245.2	−50.3	5.8	98	50	11	−11.9	3.6
Unnamed14	307.1	−1.9	5.1	142	44	4		
Unnamed15	44.8	+53.8	11.7	90	19	5		
Unnamed17	340.3	+32.5	9.7	90	11	4		
Unnamed18	225.2	−39.9	4.3	81	19	1		
Unnamed19	22.7	+8.8	11.3	106	23	5		
Unnamed20	39.9	+23.6	7.5	83	12	2		
Unnamed21	129.0	−49.2	12.8	120	20	8	−5.3	1.9
Unnamed22	72.4	+11.6	5.2	85	7	3		
Unnamed23	263.1	+4.6	9.3	115	17	4		
Unnamed24	329.8	+0.4	9.6	122	23	7	−5.5	2.1
Unnamed26	340.8	+27.4	4.8	88	7	2		
Unnamed27	18.1	−14.9	7.3	94	26	2		
Unnamed28	85.4	−22.5	7.6	103	15	6	−5.5	2.3
Unnamed30	281.4	−31.8	7.3	88	25	3		
Unnamed32	331.7	−6.2	7.9	120	37	12	−8.7	2.5
Unnamed33	12.7	−38.0	4.4	90	12	2		
Unnamed34	159.4	−42.4	8.8	166	29	12	−4.1	1.2
Unnamed35	309.2	−48.3	7.9	105	45	9	−8.5	2.8
Unnamed36	300.4	−55.6	10.4	199	116	55	−5.1	0.7
Unnamed37	285.1	−56.3	7.2	131	88	27	−8.1	1.6
Vibidia	220.5	−27.0	7.1	163	300	91	−6.6	0.7

Note. Crater and boulder diameters are D and d, respectively, and α is the power law exponent of the (cumulative) boulder SFD as derived with the ML method (only for craters with $n_{d>4px} > 5$).

where N is the number of boulders larger than d_{min}. Often used to define the Weibull distribution are the scale parameter $\lambda = \alpha^{-1/\beta}$ and shape parameter $k = \beta = 3(\gamma + 1)$. We estimate α and β from the boulder sizes $d_i > d_{min}$ using the ML method. To maximize the log-likelihood function, these two equations must be satisfied:

$$\alpha = \frac{N}{\sum\left(d_i^\beta - d_{min}^\beta\right)}$$

$$\frac{N}{\beta} + \sum \ln d_i - N \frac{\sum\left(d_i^\beta \ln d_i - d_{min}^\beta \ln d_{min}\right)}{\sum\left(d_i^\beta - d_{min}^\beta\right)} = 0. \tag{11}$$

We find $\hat{\beta}$ from a simple grid search and $\hat{\alpha}$ by inserting $\hat{\beta}$. The Weibull distribution is also discussed by Clauset et al. (2009) as the "stretched exponential" distribution.

3. Results

3.1. General Statistics

Boulders on Vesta come in many shapes and sizes. In total, we identified 6,577 boulders on the surface of Vesta with a diameter larger than 3 image pixels (60 m), of which 2,318 were larger than 4 pixels (80 m). We found that all boulders are associated with impact craters, whose diameter we indicate with D. The details of all craters with at least one boulder larger than 4 pixels ($n = 69$) are listed in Table 1. Examples of Vesta boulder morphology are shown in Figure 3, which also illustrates one of the challenging aspects
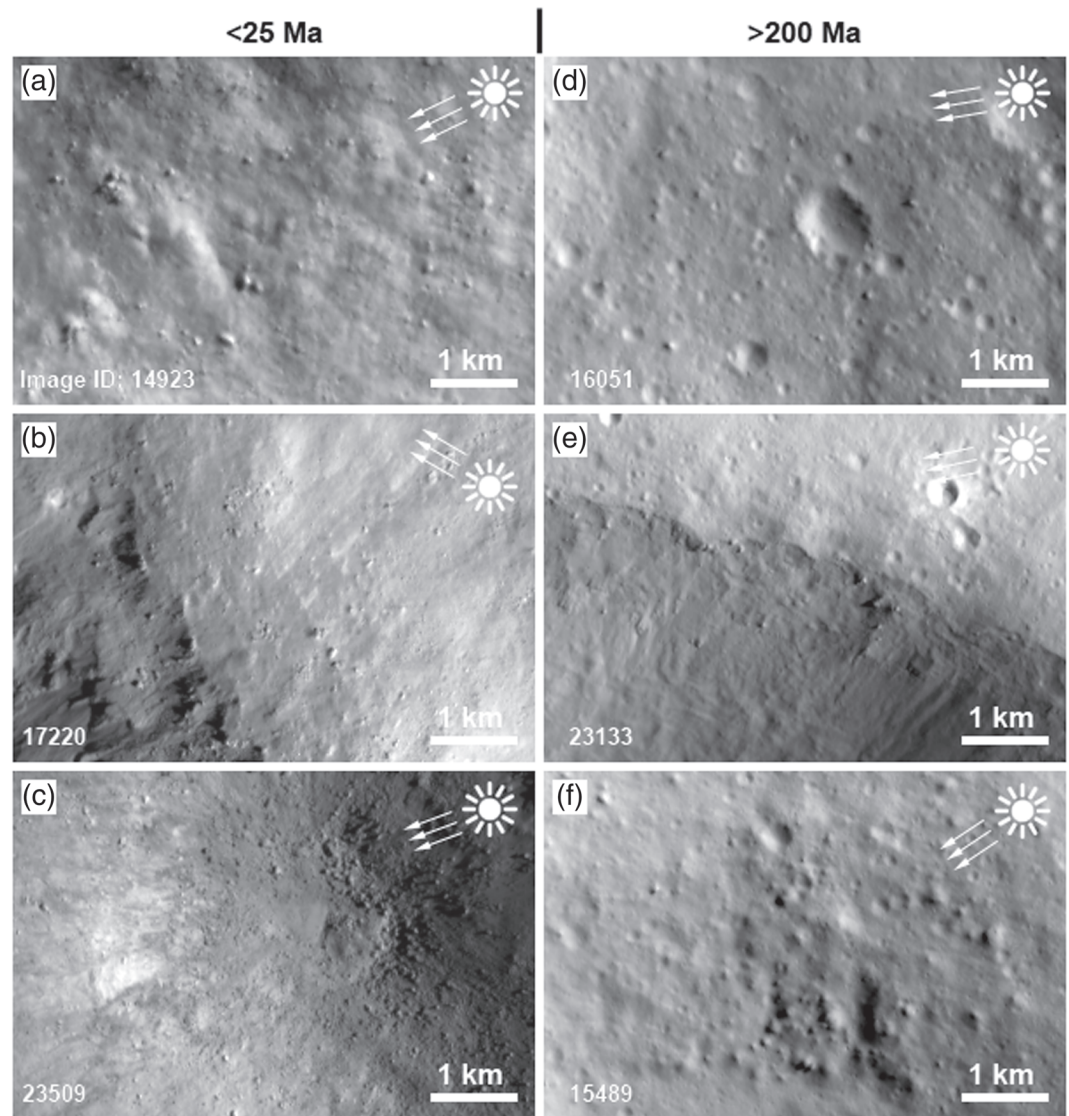
Figure 3. Examples of boulder fields associated with craters younger than 25 Ma (left side) and older than 200 Ma (right side) (ages in Table 2). North is up in all images. The illumination direction is shown at the upper right and the image number at lower left. (a) Southern (downslope) inner wall of Antonia. (b) NE rim of Cornelia and adjacent plateau. (c) Interior of Vibidia. (d) Southern part of Eusebia. (e) Northern rim of Galeria. (f) Northern interior wall of Unnamed36.

of boulder identification: Boulders change shape over time. Young craters have boulders that are easily recognized with their well-defined shadows. Old craters have only few boulders, most of which are large and rather look like mounds, with diffuse shadows. For such craters it is likely that the more numerous small boulders have simply degraded beyond recognition. We will discuss the craters in Figure 3 in more detail in section 3.3.

We summarize the general statistics of the global boulder population in Figure 4. The number of boulders per crater clearly depends on crater size (Figure 4a). The correlation is not very tight because the number also depends on crater age. The size of the largest boulder of a crater (diameter L) depends on the crater size too (Figure 4b). In contrast to the number of boulders, the size of the largest boulder does not necessarily depend on age, as boulders may disintegrate in place to form equally sized mounds (Figure 3). Being a single measurement, the largest boulder size is a poor statistic but is nevertheless often used to characterize boulder populations. The largest boulder we identified on Vesta is around 400 m large and located on the floor of Marcia crater. The inset in Figure 4b shows the challenges of assigning a unique size to large boulders,
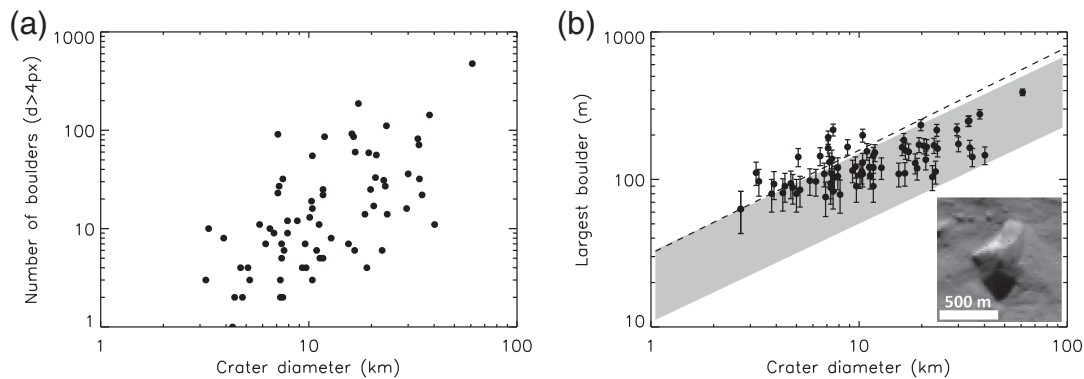
Figure 4. Basic statistics of the Vesta boulder population. (a) Number of boulders larger than 4 image pixels ($d > 80$ m) for all craters. (b) Diameter of largest boulder for these craters, assuming a measurement error of 1 pixel. The empirical range given by Moore (1971) for selected lunar and terrestrial craters is shown in gray. The dashed line is the relation given by Lee et al. (1996). The inset shows the largest boulder identified on Vesta, located on the floor of Marcia crater.

which often have an irregular shape. In the figure we simply assumed a 1 pixel measurement uncertainty, but the actual uncertainty increases with boulder size. Boulders of such huge size are unknown on Earth, but their identification on Vesta is unambiguous. Lee et al. (1986) provided a plot of the size of the largest boulder on the Moon and the Martian moons Deimos and Phobos. The Vesta largest boulder distribution agrees well with theirs where our crater size ranges overlap ($3 < D < 10$ km). In Figure 4b we also compare our distribution with the relation provided by Lee et al. (1996) ($L = 0.25D^{0.7}$ with L and D in m) and with the empirical range established by Moore (1971) for a selection of lunar and terrestrial craters ($L = 0.01^{1/3}KD^{2/3}$ with K ranging from 0.5 to 1.5). The former relation represents more or less the upper limit of the latter range. We find that the largest boulders of the smaller craters ($D < 10$ km) agree well with the Lee et al. (1996) relation, whereas the largest boulders of the larger craters ($D > 10$ km) agree better with the Moore (1971) range. But our total population of largest boulders does not agree with either relation. How uncertain are our size measurements? The first author of this paper carefully verified all largest boulders as identified by the second author. For example, there is indeed a 220 m-sized large, angular block on the rim of the 7.5 km-sized crater Unnamed12. Of course, we cannot conclude with certainty that this superblock is indeed a (former) boulder ejected by the impact that created the crater. We also note that the second-largest block around Unnamed12 is less than half the size of the largest, which is more in line with the aforementioned relations. Given the uncertainties in our method and the empirical relations, we conclude that the largest boulder sizes on Vesta agree reasonably well with what has been observed on other small bodies.

3.2. Spatial Distribution

In Figure 5, we plot the distribution of all boulders on the surface of Vesta with a size of at least 3 pixels on an albedo map. Our map differs from the craters-with-boulders map of Denevi et al. (2016), because of our restriction on boulder size and their restriction on crater size (<12 km diameter). The largest crater on Vesta with boulders, Marcia, dominates the center of the map. Even though the count of 3 pixel-sized boulders is most likely incomplete (see section 3.4.1), we nevertheless chose to display these instead of 4 pixel-sized boulders, as there are relatively few of the latter. First we note that the boulder count is incomplete for craters at high latitudes in the Northern Hemisphere, because their floors were mostly in the shadow during LAMO. South of 50°N, the spatial distribution of craters with boulders appears not to be entirely random. The albedo map gives the impression that boulders tend to avoid a large area of below-average albedo, color-coded blue, which was also noticed by Denevi et al. (2016). The dark material in this area may have been delivered by a large carbonaceous chondrite impactor that created the ancient Veneneia basin (Jaumann et al., 2014; Prettyman et al., 2012; Reddy et al., 2012). The ejecta of the other large basin on the south pole, Rheasilvia, are distributed over the entire Southern Hemisphere (Yingst et al., 2014). Craters with boulders dot the Southern Hemisphere, and there is no obvious north-south gradient in the abundance of such craters. Therefore, the scarcity of craters with boulders on dark terrain may be related to the, presumably carbonaceous, composition or the fact that these are former ejecta. Boulders may form less easily here; Denevi et al. (2016) suggested that the regolith is thicker than average or live shorter. These ideas can be tested by studying the boulder population of Ceres, Dawn's next mission target, whose reflectance spectrum is similar to that of carbonaceous chondrites (McCord & Gaffey, 1974). Marcia, which is located within the dark terrain, has
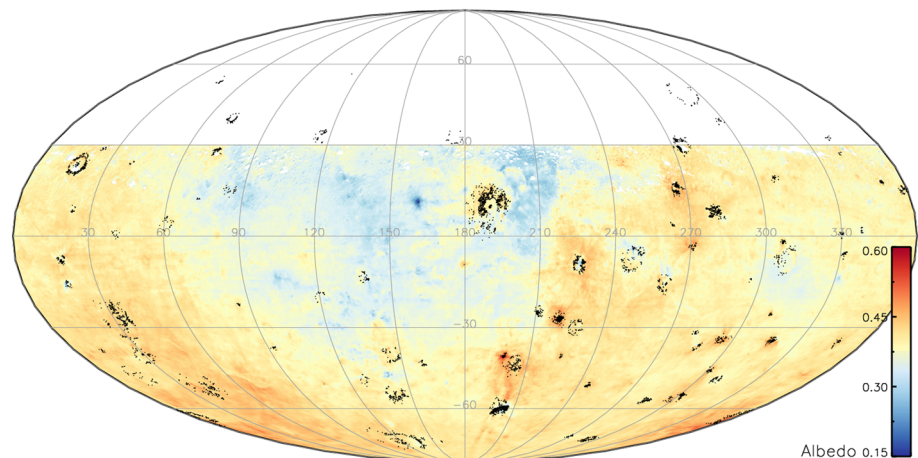
Figure 5. Distribution of all boulders (black dots) identified on Vesta with a size of at least 3 pixels ($d > 60$ m) displayed on a normal albedo map from Schröder et al. (2013).

abundant boulders. As the dark layer is relatively thin (Jaumann et al., 2014), the impactor that formed Marcia likely punched through it, and the boulders are composed of the underlying, nondark material.

The distribution of boulders in and around the craters on Vesta is highly variable. We show the boulders distribution for a selection of craters in Figure 6. Some craters have most boulders located outside the rim (Cornelia and Licinia); others have most boulders located inside the crater (Marcia and Vibidia). Boulders associated with craters that formed on a slope (Krohn et al., 2014) are concentrated on the downslope side of the crater (Antonia and Unnamed36). We plot the boulder locations in two colors: green for boulders with a size between 3 and 4 pixels and red for boulders larger than 4 pixels. The figure shows that boulders of this size ($d > 60$ m) are generally found within one crater diameter of the rim. Rarely did we find boulders further away; in such cases the identification was invariably ambiguous. We expect that large boulders are found closer to the crater rim than smaller boulders because of the larger amount of energy required to eject them, a prediction confirmed for lunar craters (Bart & Melosh, 2010; Krishna & Kumar, 2016; Pajola et al., 2019). However, the red and green boulders in Figure 6 are not clearly segregated in terms of distance from the crater center. A clear correlation between boulder size and distance from the crater was not found for Ceres either (Schulzeck et al., 2018). But it is still possible that such a correlation exists for Vesta and that we failed to find it only because boulders smaller than 60 m could not be reliably identified. The number of boulders around each crater depends not only on the crater size but also on age. We discuss the latter dependency in the following section.

Figure 6 does not distinguish between boulders inside and outside the crater rim. We found little evidence for the production of boulders by physical weathering from crater walls. Rock falls can be triggered by thermally induced mechanical stresses due to varying insolation (do Amaral Vargas et al., 2013). However, we could not identify any boulder tracks on the talus material that mantles many inner crater walls, in contrast to the Moon where boulder tracks are common (Bickel et al., 2019; Senthil Kumar et al., 2016). We also analyzed the distribution of boulders with respect to the local slope. The boulder density is low on steep slopes, as expected, but there is no systematic increase of boulder density at the foot of steep slopes, which would be expected if physical weathering recently produced new boulders here. This lack of evidence for the production of boulders larger than 60 m by postimpact weathering is consistent with the notion of Denevi et al. (2016) that boulders on Vesta are excavated from bedrock or regolith by impacts. As boulders on Vesta appear to be the direct result of a single geologic process, that is, impact cratering, we do not distinguish boulders located inside and outside of craters in the remainder of this paper. This also resolves the complication that "inside" and "outside" are poorly defined for craters that formed on a slope (Krohn et al., 2014).

3.3. Boulder Lifetime

Boulders degrade over time and eventually disappear from the surface. Two mechanisms thought to be responsible for boulder decay on asteroids are collisional fragmentation by meteorite impact and thermal fatigue (Delbo et al., 2014; Basilevsky et al., 2015). On Vesta we expect collisional fragmentation to dominate
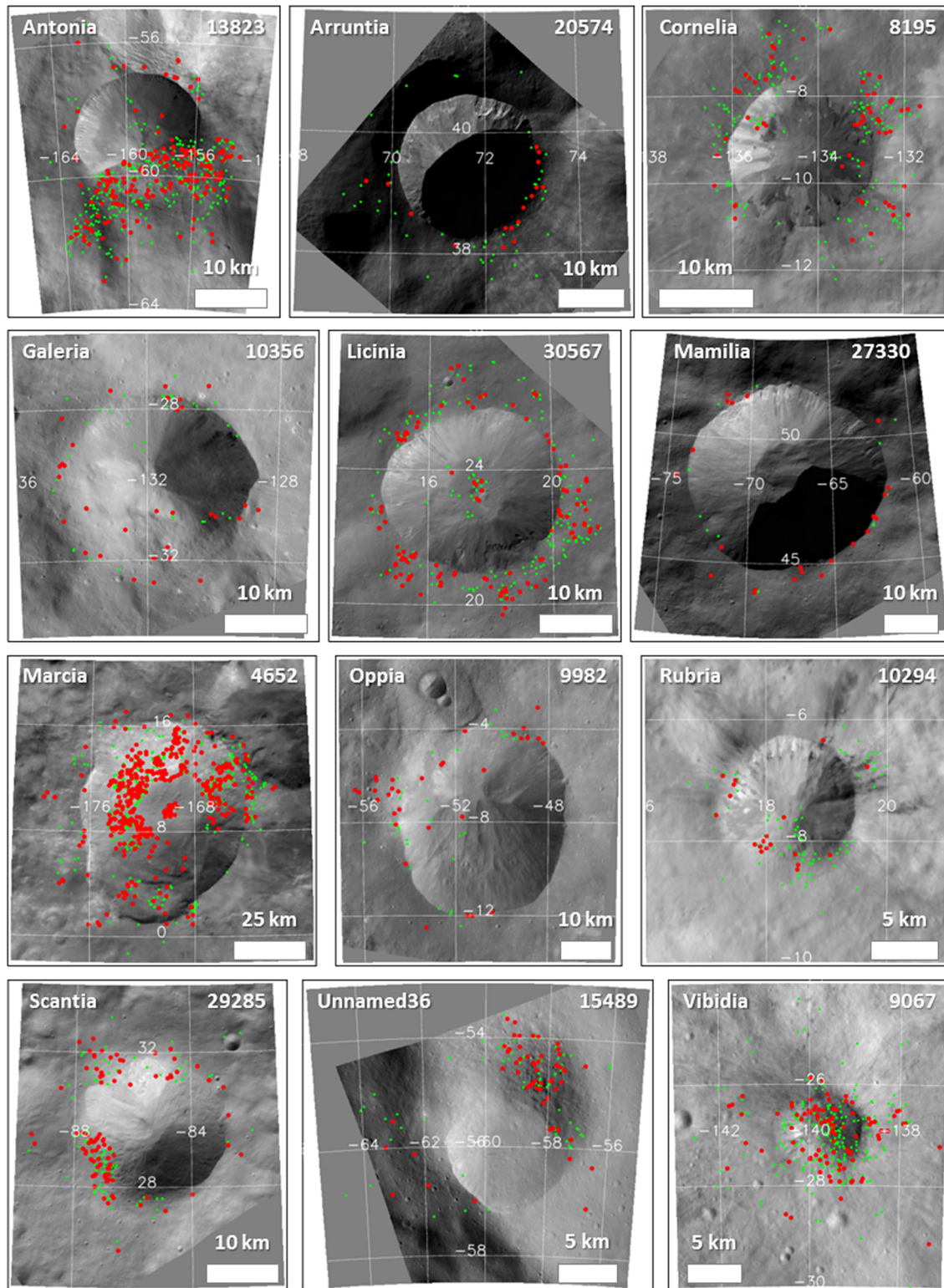
Figure 6. Boulders around craters for which an age estimate is available (Table 2). Green, small dots represent boulders with a size between 3 and 4 pixels (60 m $< d <$ 80 m). Red, large dots represent boulders larger than 4 pixels ($d >$ 80 m). The image number is indicated in the top right.

Table 2
*Age and Boulder Density for Craters for Which an Age Estimate Is Available*

Name	Age (Ma)	Density (km^{-2})	Source for age
Antonia	19–23	2.1 ± 0.1	Schmedemann et al. (2014)
Arruntia	2–3	(0.71 ± 0.09)	Ruesch et al. (2014)
Cornelia	9–14	1.01 ± 0.07	Krohn et al. (2014)
Eusebia	208–221	0.31 ± 0.03	Kneissl et al. (2014)
Galeria	209–241	0.17 ± 0.02	Kneissl et al. (2014)
Licinia	45–54	0.64 ± 0.04	Ruesch et al. (2014)
Mamilia	164–188	(0.039 ± 0.006)	Ruesch et al. (2014)
Marcia	120–149	0.33 ± 0.01	Williams, Denevi, et al. (2014)
Oppia	309–331	0.072 ± 0.009	Schmedemann et al. (2014)
Rubria	14–23	1.16 ± 0.12	Krohn et al. (2014)
Scantia	129–149	0.86 ± 0.06	Ruesch et al. (2014)
Unnamed36	240–270	1.37 ± 0.13	Krohn et al. (2014)
Vibidia	9–11	7.6 ± 0.4	Kneissl et al. (2014)

Note. Density is defined as the number of boulders larger than 3 pixels divided by crater equivalent area. The densities in brackets are underestimates, as the associated craters were largely in the shadow in LAMO images.

because the consequences of the diurnal cycle are probably too small, mainly because of the large distance from the Sun (Molaro & Byrne, 2012; Basilevsky et al., 2015; Molaro et al., 2017). By comparing the boulder abundance with a crater's age, we can estimate the typical boulder survival time. Basilevsky et al. (2015) predicted that the boulder survival time on Vesta is much smaller than on the Moon, based on estimates of the potential impactor flux and the expected impact velocities. The expected boulder survival time scales with the inverse of the impact energy, which scales as the impactor flux times the square of the impact velocity. The authors used all known orbits of minor bodies in the inner solar system to estimate the flux of potential boulder-destroying impactors, which are too small to be observed. The impactor flux predicted in this way for Vesta is about 300 times larger than that for the Moon. The typical impact velocity on Vesta is about a third of that on the Moon. So the estimated boulder survival time on Vesta is about 9/300 = 0.03 times that on the Moon, that is, 30 times shorter. Age estimates derived from crater counting are available for some Vesta craters with boulders, so we can test this hypothesis.

Two alternative chronologies exist for Vesta (Williams, Jaumann, et al., 2014): the model of Schmedemann et al. (2014), based on the lunar-derived crater production and chronology functions, and the (Marchi et al., 2014; O'Brien et al., 2014) model, with crater production and chronology functions derived from models of asteroid belt dynamics. For this paper we accept the Schmedemann et al. (2014) chronology, not because we necessarily believe it is to be preferred over the other but because more ages based on this model are available in the literature. Table 2 lists the estimated ages of the craters shown in Figure 6, together with the areal density of their boulders. The ages span a range of 2 Ma to more than 300 Ma. For these craters, the Schmedemann et al. (2014) chronology yields lower ages than the (Marchi et al., 2014; O'Brien et al., 2014) chronology (Kneissl et al., 2014), so the tabulated ages are conservative estimates. The tabulated areal density is defined as the total number of boulders identified in and around a crater divided by the crater area, which is calculated as the area of a circle with the diameter for that crater. Figure 7 shows how the boulder density varies with crater age. Assuming that the initial boulder density is similar for all craters, the figure confirms the expected correlation of density with age. The figure is for boulders with a minimum size of 3 pixels, but the results are similar for a minimum size of 4 pixels. Some data points in the figure are less reliable than others. The boulder count is incomplete for craters at high latitudes in the Northern Hemisphere, and craters whose boulder densities are consequently underestimated are Arruntia, Mamilia, and Scantia (open symbols in Figure 7a). Crater Unnamed36 has a much higher boulder density than expected for its age of about 250 Ma. This crater is an outlier for two possible reasons: First, the age estimate is based on a small number of craters (<50) and may not be fully reliable for the same reason that power law exponents derived from boulder populations of small size are not reliable. Second, it is not clear whether some of the larger
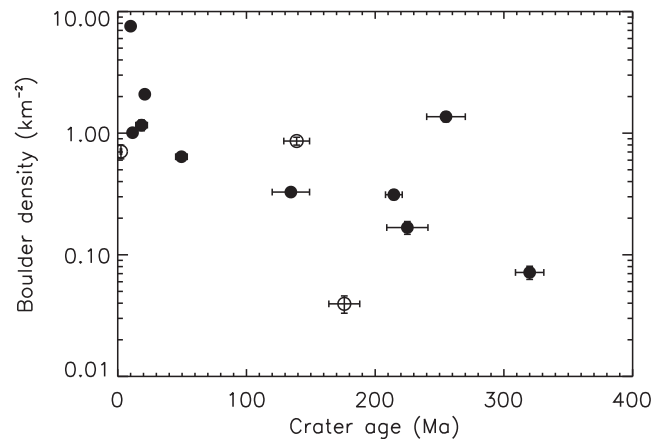
Figure 7. The density of boulders larger than 3 pixels ($d > 60$ m) versus crater age (Table 2). The error bars on the density were calculated assuming the number of boulders follows a Poisson distribution. The open symbols represent craters whose boulder density is underestimated because they were largely in the shadow in LAMO images.

mounds that we identified as degraded boulders were once truly boulders or have always been mounds of rubble, as the high abundance of suspected boulders may be related to the fact that this crater formed on a slope (Krohn et al., 2014). The oldest crater for which we identified boulders is Oppia, with an age of 320 ± 24 Ma (Schmedemann et al., 2014). We did not find boulders around Octavia crater (147°E, −3°), whose age is estimated as 390 ± 28 Ma by Schmedemann et al. (2014) and 280–360 Ma by Williams, Denevi, et al. (2014). Then, the maximum age of large boulders (>60 m) appears to be around 350 Ma.

The Vesta boulder density-age relation compares well to that for boulders on the Moon shown in Basilevsky et al. (2015), who wrote that after "a few million years, only a small fraction of meter-sized [lunar] boulders are destroyed but after several tens of million years ~50% are destroyed, and for times of 200–300 Ma, ~90 to 99% of the original boulder population is obliterated." Judging from Figure 7, this statement also perfectly applies to Vesta boulders, where we note that the scatter in the Vesta data is large, but of the same order as that in the lunar data shown in Basilevsky et al. (2015). Because the ages based on the Schmedemann et al. (2014) chronology are conservative estimates, we conclude that the boulder survival time on Vesta is at least as long as that on the Moon. The Basilevsky et al. (2015) prediction appears to be incorrect by more than a factor 30. What can explain the discrepancy? For a start we will assume that Vesta boulders are not more resistant to degradation than lunar boulders given their similar composition and that both available Vesta chronologies do not dramatically overestimate the crater ages. The impact velocities seem to be uncontroversial, as O'Brien and Sykes (2011) arrive at similar values as Basilevsky et al. (2015). The meteorite flux as estimated by Basilevsky et al. (2015) from asteroid orbits as published by the Minor Planet Center is very similar for Vesta and Ceres, and about 300 times larger than on the Moon. In a similar exercise, O'Brien and Sykes (2011) find the impact probability for Ceres to be about 25% higher than for Vesta because of the former's more central location in the main asteroid belt but do not provide an impact probability for the Moon. Then the most likely reason for the discrepancy is probably the difference in scale. The lunar boulders considered by Basilevsky et al. (2015) are typically less than 10 m in size, whereas our Vesta boulders are sized between 60 and 400 m. The implication is that the flux of impactors that can destroy 10 m-sized boulders on Vesta is about 30 times larger than the flux of impactors that can destroy 100 m-sized boulders.

3.4. Size-Frequency Distribution

3.4.1. Vesta

First, we pool all boulders counted on the surface of Vesta to find the (cumulative) power law exponent of the global boulder population. Figure 8 shows the SFD, both in cumulative and differential representation. At the top of the differential plot we show the implications of a 1 pixel measurement error on a logarithmic scale. We chose a logarithmic bin size of 0.07 with the boulder size in meters, ensuring that the size is on the order of the measurement error at the larger end of the scale. As the error is larger than the bin size at the smaller end of the scale, we can expect boulders to spill over into adjacent bins merely by chance. We recognize the characteristic downturn ("rollover") of the distributions toward smaller diameters, caused by the limited spatial resolution and the measurement error.
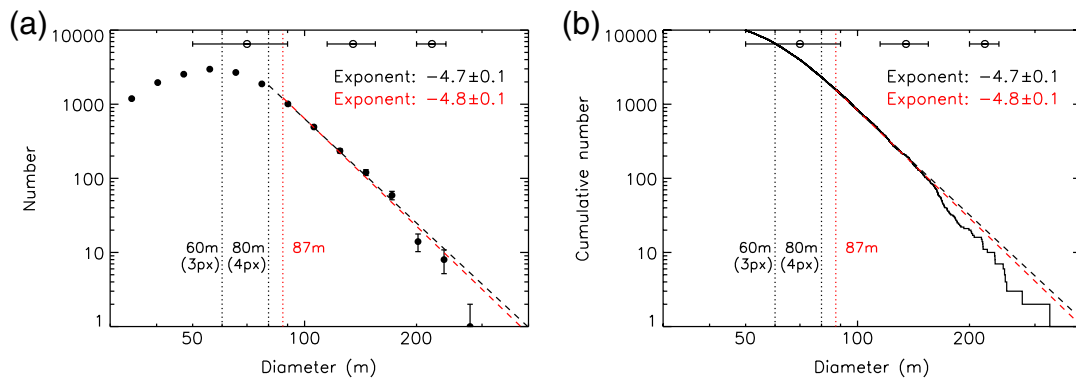
Figure 8. The SFD of all boulders identified on Vesta, displayed both in differential (a) and cumulative (b) format. Different size limits are indicated by vertical (dotted) lines. The dashed lines are best fit power laws using the ML method, with exponent indicated: The black dashed line has d_{min} = 80 m (4 pixels), whereas the red dashed line has d_{min} = 87 m, as estimated by the ML algorithm. The error bars at the top indicate the uncertainty in boulder size at different diameters due to a 1 pixel measurement error.

We fit two power laws to the data with the ML method, one with the minimum boulder size (d_{min}) fixed and the other with d_{min} estimated by the ML algorithm. When fixing d_{min} to 4 pixels (80 m), we find a power law exponent of $\alpha = -4.7 \pm 0.1$ ($n = 2,319$, black line in Figure 8). By extrapolating this power law to smaller diameters, we find that the number of boulders with a diameter of around 3 pixels may be severely underestimated; the observed number in the 3 pixel bin is about 3,000, but the extrapolated, expected number is more like 7,000. The counts for boulders larger than 4 pixels are probably close to complete. We note that the counts at the largest diameters do not match well with the power law, both in the cumulative and differential representation. Alternatively, when we let the ML algorithm choose the minimum boulder size, we find d_{min} = 87 m and a slightly steeper power law with $\alpha = -4.8 \pm 0.1$ ($n = 1,575$, red line in Figure 8). The minimum boulder size is close to our earlier estimate of 80 m, confirming that 4 pixels is a reasonable lower limit for the size. But also, this power law does not match the counts at large diameters. In fact, the statistical test provided by Clauset et al. (2009) indicates that neither power law in Figure 8 is a good model for the data ($p = 0$ and 0.02, respectively).

We also estimated the power law exponent for each crater individually for craters with at least six boulders with a diameter larger than d_{min} = 80 m. Plotting these exponents as a function of number of boulders in the population in Figure 9, we find a strong negative bias for smaller populations, which we expected from the generic simulation in Figure 2. We also include three simulations in Figure 9 that use the observed population sizes and adopt the best fit power law exponent for the global boulder population ($\alpha = -4.7$, d_{min} fixed). When we compare the simulations with the observations we notice two things: First, the observed exponents of craters with small boulder populations are typically more negative than in the simulations. Second, the power law exponent of the crater with the largest number of boulders, Marcia, is far from -4.7, even though the simulated "Marcia's" invariably have exponents close to -4.7. This suggests that Marcia's actual exponent significantly differs from that of the global boulder population. We can already see this in Figure 6, where the ratio of large to small boulders in Marcia is comparatively high. The reason for this is not obvious. There is ample evidence for flows inside and outside the crater (Williams, Denevi, et al., 2014), so perhaps small boulders were preferentially buried. It is also possible that, because of Marcia's large size, its boulders originate in a deeper, mechanically stronger or less fragmented layer in the interior, making them more resistant to degradation. When we exclude Marcia's boulders from the global population, we derive an exponent of $\alpha = -5.1 \pm 0.1$ (d_{min} = 80 m, $n = 1,843$, black line in Figure 10), which means a steeper power law. The best fit power law better fits the observed distributions in the 80–180 m range, although the number of large boulders still appears too low. We repeat our simulations with this revised exponent in Figure 11. Now the observed exponents of craters with small numbers of boulders agree better with those in the simulations. This reinforces the notion that the Marcia boulder population is different from that of all other craters. When we let the ML algorithm estimate the minimum boulder size, we find d_{min} = 91 m and an even steeper power law with $\alpha = -5.4 \pm 0.2$ ($n = 1,023$, red line in Figure 10). Still, the Clauset et al. (2009) test indicates that neither power law is an acceptable model for the data ($p = 0$ and 0.007, respectively). Then also, without the Marcia boulders, there is no single power law that fits the global distribution over the whole size range.
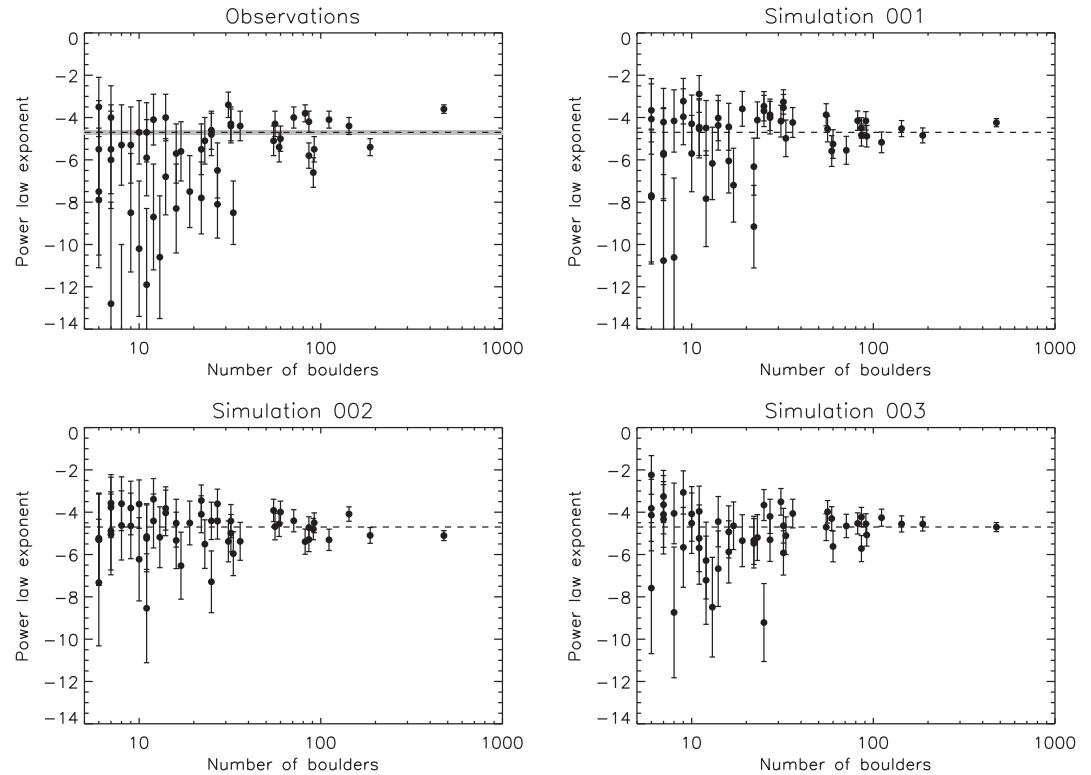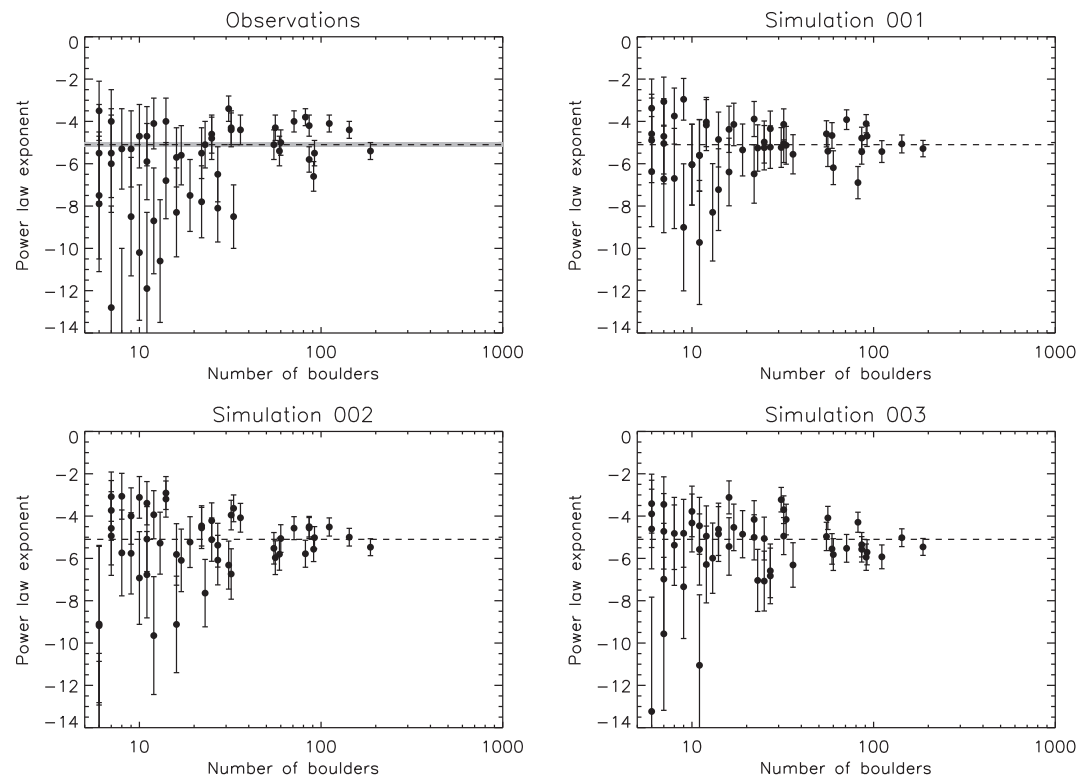
Figure 9. Power law exponents for all craters with a population of at least six boulders larger than 4 pixels ($n = 52$). The observed exponents were derived by fitting a power law to the data of each crater. The best fit power law index for the observed global boulder distribution is $\alpha = -4.7 \pm 0.1$ (dashed line with gray confidence interval). The crater with the largest number of boulders (548) is Marcia. We compare the observations to three simulations. The simulated exponents were derived by fitting randomly generated boulder distributions, assuming a Pareto distribution with $\alpha = -4.7$ (dashed line), using the number of boulders in the population of each crater as input.

The failure of the power law to describe the SFD leads us to the Weibull distribution. The question is now whether to include Marcia boulders or not. If the boulder sizes are distributed according to a power law, then exclusion is justified, but the situation is not so clear if we assume a Weibull distribution. We therefore show the best fit left-truncated Weibull distribution (Equation 10) in Figure 12, both with (a) and without (b) Marcia boulders. Again, we restrict the fit to boulders of size >4 pixels. Including all boulders, the best fit distribution has $N = 2,319$, $\alpha = 2.25$, and $\beta = 0.37$ (scale parameter $\lambda = 0.11$ and shape parameter $k = 0.37$). Without Marcia boulders, the best fit parameters are $N = 1,843$, $\alpha = 0.69$ m, and $\beta = 0.56$ (scale parameter
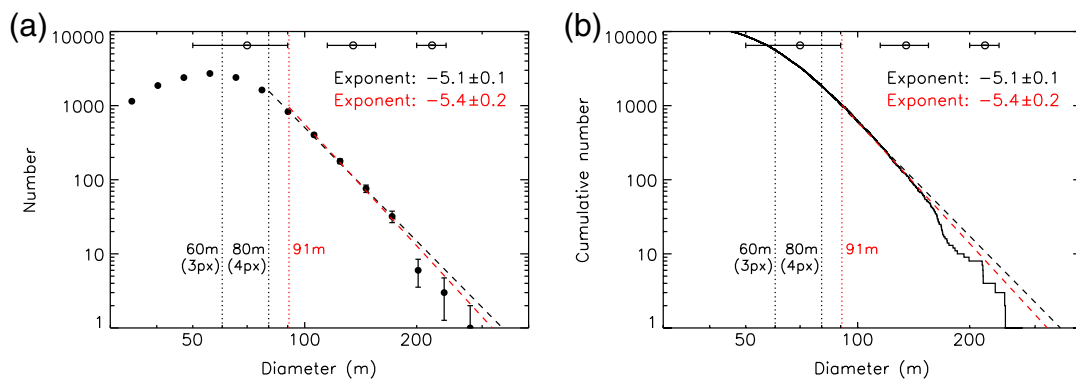
Figure 10. The SFD of all boulders identified on Vesta, excluding those of Marcia, displayed both in differential (a) and cumulative (b) format. Different size limits are indicated by vertical (dotted) lines. The dashed lines are best fit power laws using the ML method, with exponent indicated: The black dashed line has $d_{min} = 80$ m (4 pixels), whereas the red dashed line has $d_{min} = 91$ m, as estimated by the ML algorithm. The error bars at the top indicate the uncertainty in boulder size at different diameters due to a 1 pixel measurement error.

Figure 11. Power law exponents for all craters with a population of at least six boulders larger than 4 pixels, excluding Marcia crater ($n = 51$). The observed exponents were derived by fitting a power law to the data of each crater. The best fit power law index for the observed global boulder distribution minus Marcia is $\alpha = -5.1 \pm 0.1$ (dashed line with gray confidence interval). We compare the observations to three simulations. The simulated exponents were derived by fitting randomly generated boulder distributions, assuming a Pareto distribution with $\alpha = -5.1$ (dashed line), using the number of boulders in the population of each crater as input.

$\lambda = 1.9$ and shape parameter $k = 0.56$). The fractal dimension $D_f = 3 - \beta$ for the cracks in the rock is 2.6 and 2.4, respectively. Excluding Marcia boulders changes the Weibull parameters but does not improve the fit to the data. The Weibull distribution fits the Vesta SFD better than the power law. And contrary to the power law, it does not imply that the number of boulders with a size of 3 pixels is massively underestimated, which seems more reasonable. The Weibull distribution is likely also a better model for the SFD of individual craters. Using the Clauset et al. (2009) test with $d_{min} = 80$ m, we found that the power law fails to fit the SFD of all four craters with more than 100 boulders larger than 4 pixels (Antonia, Licinia, Marcia, and Pinaria).

3.4.2. Other Small Bodies

How does the Vesta boulder SFD compare to those of boulder populations on other small Solar System bodies? In the literature, the boulder SFD distribution is generally assumed to follow a power law. Several authors have now used the ML method to estimate the power law exponent.

3.4.2.1. (25143) Itokawa

DeSouza et al. (2015) determined the exponent for the global block distribution of S-type asteroid Itokawa to be $\alpha = -3.6 \pm 0.3$, based on a sample of about 800 boulders from Mazrouei et al. (2014) in the size range of 7–35 m (using the equivalent spherical radius method for sizing the boulders). Michikami et al. (2019) confirmed this value as -3.5 ± 0.2 in an analysis based on the same measurements. The total number of boulders is large enough to conclude that the Itokawa power law exponent is significantly different from that of Vesta. However, Itokawa is different from Vesta and the other bodies considered in this section, in the sense that its boulders are not associated with particular craters but are thought to all derive from the disruption of a parent body (Michikami et al., 2008; Nakamura et al., 2008).

3.4.2.2. (1) Ceres

Schulzeck et al. (2018) determined the exponent for a number of craters on dwarf planet Ceres and found values in the range of -6.2 to -4.4. The most reliable value was that obtained for Jacheongbi crater:
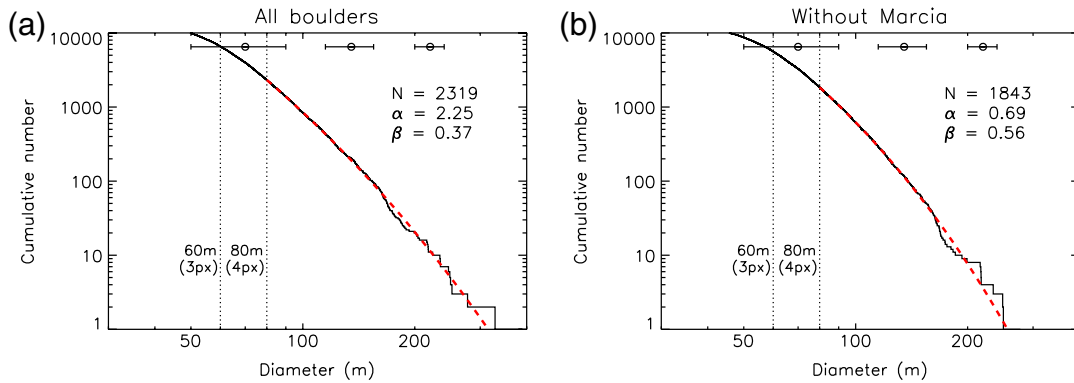
Figure 12. Left-truncated Weibull distribution for Vesta boulders larger than 4 pixels, with (a) and without (b) Marcia boulders, displayed in cumulative format. The parameters of the best fit distribution (red curve) are listed. The error bars at the top indicate the uncertainty in boulder size at different diameters due to a 1 pixel measurement error.

$\alpha = -4.4 \pm 0.7$, with 147 boulders in the 162–400 m size range, which is not significantly different from the Vesta exponent. More negative values were determined for other craters with fewer boulders, which is consistent with the negative bias at small boulder numbers we observed in our simulations. We pooled all boulder counts from Schulzeck et al. (2018) (six craters) and determined the power law exponent using two methods to choose d_{min}: (1) setting it to 4 pixels and (2) estimating it by means of the ML algorithm. Figure 13 shows the results in the differential (a) and cumulative (b) representations. For 1, we find an exponent of -4.3 ± 0.2 from measurements of 544 boulders in the 140–394 m size range. For 2, we determined an exponent of -5.6 ± 0.4 from measurements of 159 boulders in the 189–394 m size range. In both cases, the Clauset et al. (2009) test indicates that a power law is not a good model for the data. The shape of the Ceres boulder SFD is similar to that of Vesta in Figure 10, and we suspect that the Weibull distribution may also be a reasonable model for Ceres.

3.4.2.3. (162173) Ryugu

Michikami et al. (2019) determined the exponent for the global block distribution of C-type asteroid Ryugu to be $\alpha = -2.65 \pm 0.05$, based on a sample of over 3,000 boulders. The authors also analyzed populations of smaller objects, like cobbles and pebbles, in individual high-resolution images and found these to have smaller exponents (around -2). This was taken as evidence for some boulders to be buried in finer particles. Ryugu's exponent for the global boulder population is significantly different from that of Vesta. Like Itokawa, Ryugu's boulders are thought to all derive from the disruption of a parent body.

3.4.2.4. (101955) Bennu

DellaGiustina et al. (2019) determined the exponent for the global block distribution of B-type asteroid Bennu to be $\alpha = -2.9 \pm 0.3$, based on a sample of about 350 boulders. Bennu's exponent is significantly
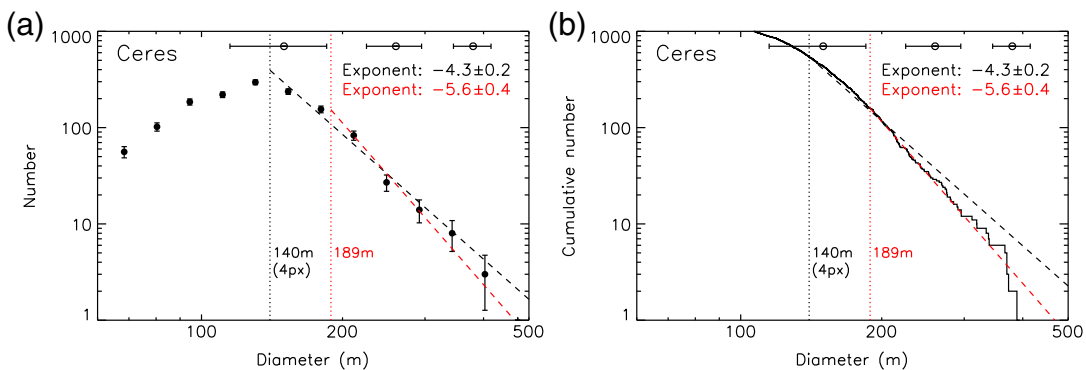
Figure 13. Power law exponent for Ceres boulders. (a) The differential distribution of all boulders counted on Ceres by Schulzeck et al. (2018). The black dashed line is the best fit power law found when adopting a minimum boulder size of 4 pixels (black vertical dotted line). The red dashed line is the best fit power law found with the minimum boulder size estimated by the ML method (red vertical dotted line). (b) As (a) but for the cumulative distribution. The error bars at the top indicate the uncertainty in boulder size at different diameters due to a 1 pixel measurement error.

different from that of Vesta. Like Itokawa and Ryugu, Bennu is a suspected rubble-pile, and its boulders are thought to all derive from the disruption of a parent body.

Other power law exponents for boulder distributions in the literature were derived from conventional methods like fitting the binned cumulative distribution. We must assess these exponents in light of the results of our simulations. Those derived by fitting the cumulative distribution may not be directly comparable. But those derived by fitting to a differential distribution should be comparable if the number of boulders included in the fit is large enough ($n > 100$).

3.4.2.5. (4179) Toutatis

Jiang et al. (2015) analyzed the boulder distribution on bilobed, S-type asteroid Toutatis. They reported an exponent of -4.4 ± 0.1 for a conventional power law fit to the binned cumulative distribution. The rollover of their cumulative distribution due to the image resolution starts around a boulder size of 25 m, which corresponds to about 70 boulders of reliable size in the 25–61 m range, which may be too few for a reliable estimate, and thus, the uncertainty is almost certainly too small. The authors also considered the boulder populations of each lobe individually and found two apparently significantly different exponents. Our simulations (Figure 2) show that the derived exponents of populations of about 30–40 boulders may be very different simply by chance, both when using the ML method and fitting the differential distribution. We are unable to assess the situation for the method of fitting the binned cumulative distribution, as there is no correct way of doing that, but we expect a similar degree of inaccuracy. Therefore, the two exponents may not be significantly different in reality.

3.4.2.6. (21) Lutetia

Küppers et al. (2012) determined an exponent of -4 for asteroid Lutetia based on a conventional power law fit to the differential distribution (the authors quoted a value of -5, but their bin size was constant on a linear rather than logarithmic scale). However, this value is essentially meaningless when considered in isolation, as their sample comprised only six boulders larger than 4 OSIRIS image pixels (240 m; compare the simulation in Figure 2b).

3.4.2.7. Phobos

Thomas et al. (2000) counted boulders on the Martian moon Phobos. They found most to be associated with Stickney crater, although this was questioned by Basilevsky et al. (2014), who suggested the age of Stickney to be much larger than the survival time of the boulders. Thomas et al. (2000) obtained an exponent of -3.2 by fitting the cumulative distribution of all boulders they identified. We reanalyze their counts by means of the ML method. First, we note that the full data set of Thomas et al. consists of the combined counts from two images of the Mars Global Surveyor camera with different spatial resolution. Images 50103 and 55103 have a resolution of 4.0 and 1.4 m per pixel, respectively. If we want to estimate a power law exponent that is representative for global Phobos, combining counts from images with different resolution will skew the SFD. We therefore assess the two images individually. When we apply our criterion for the minimum boulder size of 4 pixels, then Images 50103 and 55103 have 17 and 529 boulders larger than 16 and 5.6 m, respectively. If we combine the two data sets and choose a minimum size of 16 m, then only 21 boulders satisfy this criterion. Thus, only Image 55103 has a sufficiently large number of boulders to reliably retrieve the exponent. We show the SFD of boulders in Image 55103 in Figure 14. The best fit power law has an exponent of -3.8 ± 0.2. However, a power law is not the correct model for the data, as confirmed by the ML test. This is not apparent in the cumulative representation (b) but can be seen in the differential representation (a), where the values in several bins are significantly off the best fit power law curve. When we estimated d_{min} from the data (5 m), the derived power law exponent appeared much too small (-2.5), which is why we do not include this solution in Figure 14. One constraint of the Phobos data is the discrete nature of the sizes (1 m accuracy), which leads to an empty bin around 2.5 m diameter in the differential distribution (containing boulders in the 2.2–2.8 m size range) and the occurrence of steps at small diameters in the (unbinned) cumulative distribution. It may also affect the occupancy rate of bins in the differential distribution at intermediate diameters. One way to resolve this issue is to choose wider bins, but this conflicts with the image resolution of 1.4 m per pixel. We will accept the retrieved exponent for Phobos, with the caveat that a power law does not fit these data well.

3.4.2.8. (21) Eros

Thomas et al. (2001) counted boulders on the S-type asteroid Eros and found that most are associated with Shoemaker crater. They obtained an exponent of -3.2 for the global boulder population by fitting the cumulative distribution. We reanalyze their counts by means of the ML method. The Eros data set combines
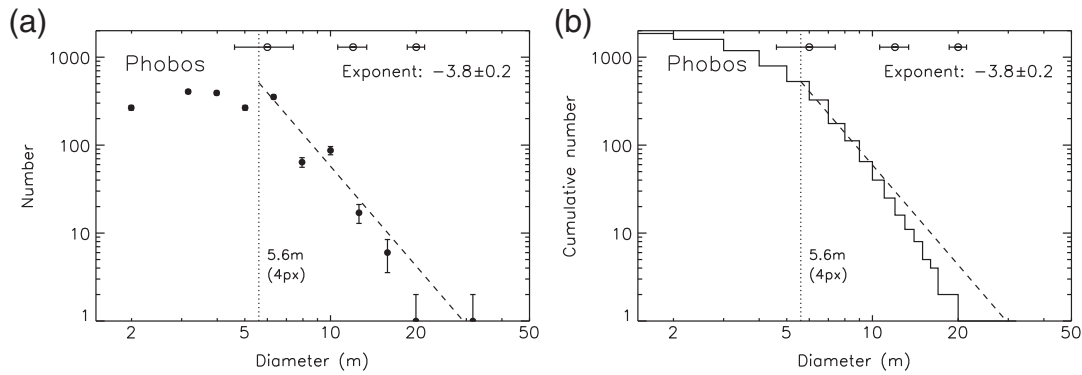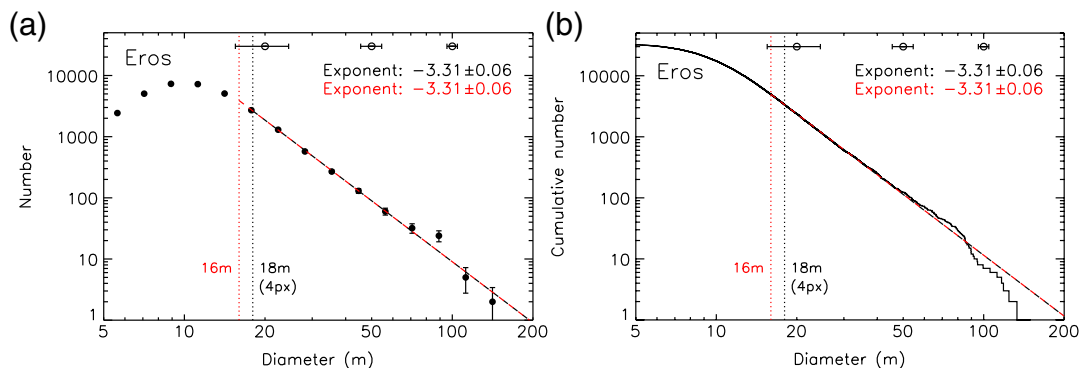
Figure 14. Power law exponent for Phobos boulders. (a) The differential distribution of all boulders counted on Phobos by Thomas et al. (2000) in Image 55103 (resolution 1.4 m per pixel). The black dashed line is the best fit power law found when adopting a minimum boulder size of 4 pixels (black vertical dotted line). (a) As (a) but for the cumulative distribution. The error bars at the top indicate the uncertainty in boulder size at different diameters due to a 1 pixel measurement error.

counts from a collection of images of the NEAR-Shoemaker camera, and most boulders were measured at spatial resolutions between 2 and 5 m per pixel (99% of the boulders were measured at a resolution <5 m per pixel). We adopt a minimum boulder size of 4.5 m per pixel, as 90% of the boulders were measured at a higher resolution than that. There are 3,347 boulders larger than the 4 pixels criterion (18 m). We show the boulder SFD in Figure 15. The best fit power law fits the data well, as confirmed by the ML test, and has an exponent of -3.31 ± 0.06. Letting the ML algorithm estimate the minimum size, it found $d_{min} = 16$ m and the same value for the exponent ($n = 4{,}850$). Because a power law describes the data so well, the ML exponent is close to the -3.2 found by Thomas et al. (2001) by fitting the cumulative distribution. Only at the largest sizes do the boulder numbers deviate from the power law curve. The authors remarked that the power law is steeper here, which we also noted for Vesta. However, as the number of boulders responsible is small (<20), the deviation may be due to chance. The large number of boulders ensures a small uncertainty in the exponent of the best fit power law, and we conclude that the Eros exponent is significantly different from that of Vesta.

3.4.2.9. The Moon

Cintala and McBride (1995) counted boulders at several Surveyor landing sites on the Moon as imaged by the Lunar Orbiter probe. Only the Surveyor VII site has boulders in the size range that we consider in this paper (>10 m). The authors fitted a power law to the cumulative SFD and found an exponent of -4.0 ± 0.1. As they provided a table of the numbers in the size bins, we can fit a power law to the differential distribution instead (Figure 16). We find an exponent of -3.6 ± 0.1, for 628 boulders in the 13–80 m size range. When comparing the boulder counts in the Lunar Orbiter images (m-sized) with counts of particles seen in Surveyor images (mm- to dm-sized) performed by Shoemaker and Morris (1968), Cintala and McBride (1995)

Figure 15. Power law exponent for Eros boulders. (a) The differential distribution of all boulders counted on Eros by Thomas et al. (2001). The black dashed line is the best fit power law found when adopting a minimum boulder size of 4 pixels (black vertical dotted line), assuming a resolution of 4.5 m per pixel. The red dashed line is the best fit power law found with the minimum boulder size estimated by the ML method (red vertical dotted line). (b) As (a) but for the cumulative distribution. The error bars at the top indicate the uncertainty in boulder size at different diameters due to a 1 pixel measurement error.
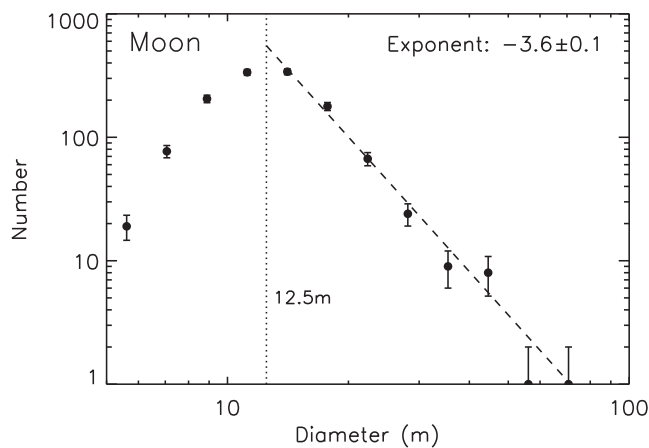
Figure 16. Power law exponent for lunar boulders: reanalyzing data for the Surveyor VII site on the Moon from Cintala and McBride (1995). The vertical dotted line is the minimum size we adopted, which is close to the quoted line pair resolution of 11 m. The dashed line is the best fit power law.

noted the smaller power law exponents associated with the latter (around −2). The discrepancy led them to suspect that the lunar particle SFD cannot be described by a single power law over the entire size range spanning 3 orders of magnitude (mm to m) and that the distribution is steeper at larger sizes. However, Li et al. (2017) revisited this topic and fitted power laws to the cumulative SFD of boulders (m-sized) near the Surveyor landing sites using Lunar Reconnaissance Orbiter images. The authors found exponents in the range of −1.5 to 3.6, consistent with Shoemaker and Morris (1968), and suggested that, in fact, a single power law can describe the lunar particle SFD over the entire size range from mm to m. Bart and Melosh (2010) fitted power laws to the cumulative distribution of boulders around 18 lunar craters and found exponents in the range of −2.2 to −5.5, with most between −3.0 and −4.5. The size range of the involved boulder populations was on the order of 1–10 m for some craters and 10–100 m for others. Krishna and Kumar (2016) fitted power laws to the cumulative SFD of large numbers of boulders around Censorinus crater, grouped according to sector, and found exponents in the range of −2.5 to −3.3, with a typical boulder size range of 2–40 m. Pajola et al. (2019) fitted a power law to the cumulative SFD of a large number of boulders around Linné crater and found an exponent of −4.0 ($n = 12{,}038$, size range 4–30 m). At the large size end of the SFD, the power law predicts more boulders than were observed. This led the authors to fit a Weibull distribution, which matched the data better. Almost all published power law exponents for lunar boulders are smaller (less negative) than that for Vesta boulders, keeping in mind that they were estimated by fitting the cumulative SFD instead of ML. The −3.6 exponent from Figure 16 seems to be typical for lunar boulders in the decameter size range.

3.4.3. Synthesis

In the previous section we evaluated, and in some cases reanalyzed, power law exponents published for boulders on small Solar System bodies. When we adopted the power law to describe the SFD of all boulders on Vesta, we found an exponent that is significantly different from that of all other bodies, with the

Table 3
Power Law Exponents Determined From Populations of at Least 100 Boulders on Small Solar System Bodies

Body	Exponent	Method	Source
Bennu	−2.9 ± 0.3	ML (d_{min} estimated)	DellaGiustina et al. (2019)
Ceres	(−4.3 ± 0.2)	ML (d_{min} = 4 px)	This work, based on Schulzeck et al. (2018)
	(−5.6 ± 0.4)	ML (d_{min} estimated)	This work, based on Schulzeck et al. (2018)
Eros	−3.31 ± 0.06	ML (d_{min} = 4 px)	This work, based on Thomas et al. (2001)
	−3.31 ± 0.06	ML (d_{min} estimated)	This work, based on Thomas et al. (2001)
Itokawa	−3.6 ± 0.3	ML (d_{min} estimated)	DeSouza et al. (2015)
	−3.5 ± 0.2	ML (d_{min} estimated)	Michikami et al. (2019)
Moon	−3.6 ± 0.1	Fitting differential	This work, based on Cintala and McBride (1995)
Phobos	(−3.8 ± 0.2)	ML (d_{min} = 4 px)	This work, based on Thomas et al. (2000)
Ryugu	−2.65 ± 0.05	ML (d_{min} estimated)	Michikami et al. (2019) (global)
	−2.07 ± 0.06	ML (d_{min} estimated)	Michikami et al. (2019) (local)
	−2.01 ± 0.06	ML (d_{min} estimated)	Michikami et al. (2019) (local)
	−1.96 ± 0.07	ML (d_{min} estimated)	Michikami et al. (2019) (local)
	−1.98 ± 0.09	ML (d_{min} estimated)	Michikami et al. (2019) (local)
	−1.65 ± 0.05	ML (d_{min} estimated)	Michikami et al. (2019) (local)
Vesta	(−4.7 ± 0.1)	ML (d_{min} = 4 px)	This work
	(−4.8 ± 0.1)	ML (d_{min} estimated)	This work

Note. Parentheses around an exponent indicate that a power law is not a good model for the data as indicated by the ML test (unavailable for the Moon).
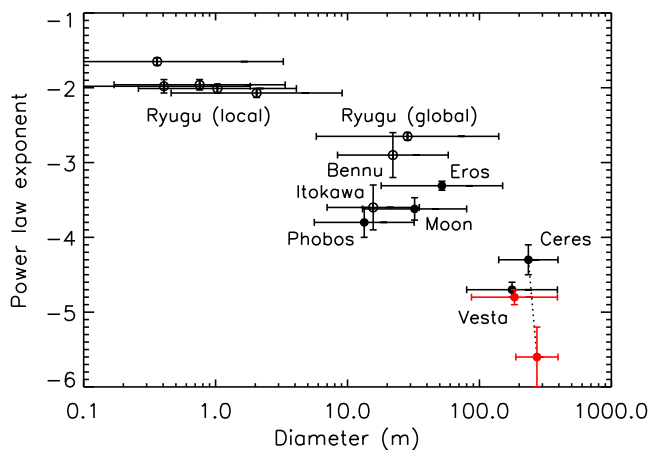
Figure 17. Power law exponent for boulders on small solar system bodies that were derived from populations of at least 100 boulders or particles (Table 3). The horizontal error bars indicate the size range over which the estimate was obtained. Open symbols are associated with suspected rubble pile asteroids. The black and red symbols for Vesta and Ceres refer to two ways of estimating $d_{\min}$ for the ML fit.

singular exception of Ceres. What is the physical meaning of this difference? In the literature, the steepness of the best fit power law is often interpreted in terms of degree of fragmentation (Krishna & Kumar, 2016; Michikami et al., 2019; Thomas et al., 2001), accompanied by a reference to Hartmann (1969), whose paper still seems to be the prime source of information on the meaning of the exponent. Hartmann (1969) found that simple fragmentation results in small exponents (−2.1 to −2.4), whereas a hypervelocity impact results in a large exponent (−3.6), where he noted that such an impact resembles extensive regrinding. Laboratory impact experiments can provide additional insight into the meaning of the power law exponent but are typically performed on scales orders of magnitude below that of the boulders we study. The type of experiment that is probably most relevant for planetary boulder formation involves impacts on semi-infinite surfaces. Buhl et al. (2014) reviewed the power law exponents derived from such experiments (Cintala et al., 1985; Fujiwara et al., 1977; Gault et al., 1963; Hörz, 1969). For particles up to a centimeter in size, the exponents were all around −2.5, regardless of the type of target material, be it sandstone, granite, basalt, or water ice. Additionally, Buhl et al. (2014) observed no correlation between the exponent and the imparted energy density (impact kinetic energy per target mass).

The authors noted that the results are different for experiments in which the entire target is disrupted, but it is unclear whether these outcomes can be extrapolated to the size range of large boulders.

While we found that the power law is not a satisfactory model for the Vesta and Ceres boulder SFDs, let us assume for the moment that it is and compare the exponents with those derived for other small solar system bodies. Table 3 lists those exponents that we consider most reliable, that is, preferably derived with the ML method from populations of at least 100 boulders. Figure 17 displays the exponents as a function of boulder size, indicating for each the size range from which it was obtained. We distinguish between boulders formed by impact on a surface and boulders that make up the rubble-pile asteroids Itokawa, Ryugu, and Bennu. Experimental evidence suggests that the SFD resulting from fragmentation of a target body is different from that resulting from an impact on a semi-infinite surface (Buhl et al., 2014). But as it is not clear whether these results can be extrapolated to planetary scales, we include rubble-pile bodies in the figure. There are two data points for both Vesta and Ceres: one for a minimum boulder size of $d_{\min} = 4$ image pixels (black symbols) and one for $d_{\min}$ estimated by the ML algorithm (red symbols). The boulders counted on Vesta and Ceres are large (>100 m), and their exponents cluster around −5. Given their very different surface composition, the similarity of the exponents is surprising. Boulders identified on other bodies are smaller (10–100 m), and their exponents are smaller too, ranging from around −3 to −4. The exponents of the rubble-pile asteroids (Bennu, Itokawa, and Ryugu) are not clearly separated from the others (Eros, Moon, and Phobos). Figure 17 also includes several exponents for Ryugu particles at small scales (<1 m), determined from individual images (Michikami et al., 2019). These exponents are smaller yet, clustering around −2, consistent with exponents derived from laboratory impact experiments (Buhl et al., 2014) and for the lunar regolith (Shoemaker & Morris, 1968). The figure shows a correlation between the exponent and the particle (boulder) size range from which it is derived.

Following Hartmann (1969), the large exponents of the SFDs of Vesta and Ceres boulders imply an extremely high degree of fragmentation. But this is difficult to understand in light of the relatively low average impact velocities expected on their surface (Basilevsky et al., 2015). The idea that extensive regrinding experienced in a hypervelocity impact leads to a power law SFD with a large exponent (Hartmann, 1969) is not supported by grinding experiments, which typically result in a Weibull distribution (Deb & Sen, 2013; Martin & Mills, 1977; Rosin & Rammler, 1933). Furthermore, Brown (1989) and Brown and Wohletz (1995) theorized that a power law distribution results from a single fragmentation event, whereas sequential fragmentation (i.e., regrinding) results in a Weibull distribution. We found that the power law is not a good model for the Vesta and Ceres boulder SFDs. However, the Weibull distribution satisfactorily fits the data. This suggests that the unusually large exponents for Vesta and Ceres should not be interpreted in terms of degree of fragmentation but simply follow from the shape of the Weibull distribution. The dependence of the power law

exponent on particle size range in Figure 17 can be understood if, in general, the particle SFD on small bodies follows a Weibull distribution over a wide range of sizes. This would provide a natural explanation for the relatively low abundance of larger boulders, which are sometimes reported as "missing" (Michikami et al., 2019; Thomas et al., 2001). The Weibull distribution has been noted before to fit the particle SFD, both at small (Martin & Mills, 1977) and large scales (Pajola et al., 2019). Over a narrow size range, the Weibull SFD may masquerade as a power law. The exponent of such a "local" power law would primarily be a function of the particle size range from which it was derived, but other factors (composition and impact velocity) may yet play a role.

4. Conclusions

We identified, counted, and measured more than 10,000 boulders on the surface of Vesta, with sizes up to several hundred meters. We found all boulders to be associated with impact craters. There is little evidence for boulder production by physical weathering of crater walls, so the vast majority of boulders were created upon impact. Craters with boulders are distributed mostly uniformly over the surface, only seeming to avoid a large area of below-average albedo. This area is believed to be rich in carbon, delivered by the primitive impactor that created the ancient Veneneia basin (Jaumann et al., 2014; Reddy et al., 2012). It is unclear why boulders are rare here; the regolith may be thicker than average (Denevi et al., 2016) or the boulders live shorter. Using published crater ages, we established that Vesta boulders have a lifetime of about a few hundred million years. This time is on the same order as that estimated for meter-sized boulders on the Moon by Basilevsky et al. (2015), who predicted that such boulders live 30 times shorter on Vesta than on the Moon. One reason for the apparent disagreement may be that the Vesta boulders in our sample are an order of magnitude larger than the lunar boulders considered by the authors.

In the literature, the SFD of planetary boulders is often fitted with a power law. Different methods to derive the power law exponent (slope) are used, but only the ML method is statistically sound (Clauset et al., 2009). We investigate how the number of boulders in a population affects the derived exponent and confirm that the ML method is biased at low numbers. The exponent is most reliably derived for a population size of at least 100 boulders, where we recommend adopting a minimum boulder size of 4 image pixels. We derived the power law exponent for all Vesta craters with boulders and find that the SFD of Marcia crater stands out as different from all others. The exponent for Vesta's global boulder population is around −5. We reviewed published exponents for small Solar System bodies. The use of different fitting techniques and limited awareness of the unreliability of small-number statistics hinder a direct comparison, and we reanalyzed several data sets. The Vesta power law slope is steeper than typically found for other small bodies. A statistical test reveals that the power law is actually not a good model for the Vesta SFD but the Weibull distribution fits the data very well. The Weibull distribution is commonly applied to describe SFDs resulting from rock grinding experiments and results from the fractal nature of the cracks propagating in the rock interior (Brown & Wohletz, 1995). The Weibull distribution may provide a better description of the SFD of boulders on small bodies than the power law and would naturally result in a steeper SFD for the relatively large boulders of Vesta.

Data Availability Statement

Dawn framing camera images are available from NASA's Planetary Data System (at https://pds.nasa.gov/). Our Vesta boulder data are available online (at https://doi.org/10.5281/zenodo.3833759).

References

Bart, G. D., & Melosh, H. J. (2010). Distributions of boulders ejected from lunar craters. *Icarus*, *209*, 337–357. https://doi.org/10.1016/j.icarus.2010.05.023

Basilevsky, A. T., Head, J. W., Horz, F., & Ramsley, K. (2015). Survival times of meter-sized rock boulders on the surface of airless bodies. *Planetary and Space Science*, *117*, 312–328. https://doi.org/10.1016/j.pss.2015.07.003

Basilevsky, A. T., Lorenz, C. A., Shingareva, T. V., Head, J. W., Ramsley, K. R., & Zubarev, A. E. (2014). The surface geology and geomorphology of Phobos. *Planetary and Space Science*, *102*, 95–118. https://doi.org/10.1016/j.pss.2014.04.013

Benedix, G. K., Lagain, A., Chai, K., Meka, S., Anderson, S., Norman, C., et al. (2020). Deriving surface ages on Mars using automated crater counting. *Earth and Space Science*, *7*, e2019EA001005. https://doi.org/10.1029/2019EA001005

Bickel, V. T., Honniball, C. I., Martinez, S. N., Rogaski, A., Sargeant, H. M., Bell, S. K., et al. (2019). Analysis of lunar boulder tracks: Implications for trafficability of pyroclastic deposits. *Journal of Geophysical Research: Planets*, *124*, 1296–1314. https://doi.org/10.1029/2018JE005876

Brown, W. K. (1989). A theory of sequential fragmentation and its astronomical applications. *Journal of Astrophysics and Astronomy*, *10*, 89–112. https://doi.org/10.1007/BF02714980

Brown, W. K., & Wohletz, K. H. (1995). Derivation of the Weibull distribution based on physical principles and its connection to the Rosin-Rammler and lognormal distributions. *Journal of Applied Physics*, *78*, 2758–2763. https://doi.org/10.1063/1.360073

Bruno, D. E., & Ruban, D. A. (2017). Something more than boulders: A geological comment on the nomenclature of megaclasts on extraterrestrial bodies. *Planetary and Space Science*, *135*, 37–42. https://doi.org/10.1016/j.pss.2016.11.006

Buhl, E., Sommer, F., Poelchau, M. H., Dresen, G., & Kenkmann, T. (2014). Ejecta from experimental impact craters: Particle size distribution and fragmentation energy. *Icarus*, *237*, 131–142. https://doi.org/10.1016/j.icarus.2014.04.039

Christensen, P. R., Engle, E., Anwar, S., Dickenshied, S., Noss, D., Gorelick, N., & Weiss-Malik, M. (2009). JMARS—A planetary GIS. AGU Fall Meeting Abstracts IN22A-06.

Cintala, M. J., Smrekar, S., Horz, F., & Cardenas, F. (1985). *Impact experiments in H_2O ice, I: Cratering* (pp. 131–132).

Cintala, M. k. J., & McBride, K. M. (1995). Block distributions on the lunar surface: A comparison between measurements obtained from surface and orbital photography (*Technical Memorandum 104804*): NASA.

Clauset, A., Shalizi, CR, & Newman, M. E. J. (2009). Power-law distributions in empirical data. *SIAM Review*, *51*(4), 661–703. https://doi.org/10.1137/070710111

Colwell, J. E. (1993). Power-law confusion: You say incremental, I say differential. In *Lunar and planetary science conference* (Vol. 24, p. 325).

Crater Analysis Techniques Working Group (1979). Standard techniques for presentation and analysis of crater size-frequency data. *Icarus*, *37*, 467–474. https://doi.org/10.1016/0019-1035(79)90009-5

Deb, D., & Sen, A. K. (2013). Rosin's law and size distribution of particles in regolith like samples—An analysis. *Planetary and Space Science*, *82*, 79–83. https://doi.org/10.1016/j.pss.2013.03.014

Delbo, M., Libourel, G., Wilkerson, J., Murdoch, N., Michel, P., Ramesh, K. T., et al. (2014). Thermal fatigue as the origin of regolith on small asteroids. *Nature*, *508*, 233–236. https://doi.org/10.1038/nature13153

DellaGiustina, D. N., Emery, J. P., Golish, D. R., Rozitis, B., Bennett, C. A., Burke, K. N., et al. (2019). Properties of rubble-pile asteroid (101955) Bennu from OSIRIS-REx imaging and thermal analysis. *Nature Astronomy*, *3*, 341–351. https://doi.org/10.1038/s41550-019-0731-1

Denevi, B. W., Beck, A. W., Coman, E. I., Thomson, B. J., Ammannito, E., Blewett, D. T., et al. (2016). Global variations in regolith properties on asteroid Vesta from Dawn's Low-Altitude Mapping Orbit. *Meteoritics and Planetary Science*, *51*(12), 2366–2386. https://doi.org/10.1111/maps.12729

DeSouza, I., Daly, M. G., Barnouin, O. S., Ernst, C. M., & Bierhaus, E. B. (2015). Improved techniques for size-frequency distribution analysis in the planetary sciences: Application to blocks on 25143 Itokawa. *Icarus*, *247*, 77–80. https://doi.org/10.1016/j.icarus.2014.10.009

do Amaral Vargas, E., Velloso, R. Q., Chávez, L. E., Gusmão, L., & do Amaral, CP (2013). On the effect of thermally induced stresses in failures of some rock slopes in Rio de Janeiro, Brazil. *Rock Mechanics and Rock Engineering*, *46*(1), 123–134. https://doi.org/10.1007/s00603-012-0247-9

Fujiwara, A., Kamimoto, G., & Tsukamoto, A. (1977). Destruction of basaltic bodies by high-velocity impact. *Icarus*, *31*, 277–288. https://doi.org/10.1016/0019-1035(77)90038-0

Gault, D. E., Shoemaker, E. M., & Moore, H. J. (1963). Spray ejected from the lunar surface by meteoroid impact (*Technical Note D-1767*): NASA.

Golombek, M., & Rapp, D. (1997). Size-frequency distributions of rocks on Mars and Earth analog sites: Implications for future landed missions. *Journal of Geophysical Research*, *102*, 4117–4130. https://doi.org/10.1029/96JE03319

Golombek, M. P., Haldemann, A. F. C., Forsberg-Taylor, N. K., DiMaggio, E. N., Schroeder, R. D., Jakosky, B. M., et al. (2003). Rock size-frequency distributions on Mars and implications for Mars Exploration Rover landing safety and operations. *Journal of Geophysical Research*, *108*, 8086. https://doi.org/10.1029/2002JE002035

Hartmann, W. K. (1969). Terrestrial, lunar, and interplanetary rock fragmentation. *Icarus*, *10*, 201–213. https://doi.org/10.1016/0019-1035(69)90022-0

Hörz, F. (1969). Structural and mineralogical evaluation of an experimentally produced impact crater in granite. *Contributions to Mineralogy and Petrology*, *21*, 365–377. https://doi.org/10.1007/BF02672808

Jaumann, R., Nass, A., Otto, K., Krohn, K., Stephan, K., McCord, T. B., et al. (2014). The geological nature of dark material on Vesta and implications for the subsurface structure. *Icarus*, *240*, 3–19. https://doi.org/10.1016/j.icarus.2014.04.035

Jiang, Y., Ji, J., Huang, J., Marchi, S., Li, Y., & Ip, W.-H. (2015). Boulders on asteroid Toutatis as observed by Chang'e-2. *Scientific Reports*, *5*, 16029. https://doi.org/10.1038/srep16029

Kneissl, T., Schmedemann, N., Reddy, V., Williams, D. A., Walter, S. H. G., Neesemann, A., et al. (2014). Morphology and formation ages of mid-sized post-Rheasilvia craters—Geology of quadrangle Tuccia, Vesta. *Icarus*, *244*, 133–157. https://doi.org/10.1016/j.icarus.2014.02.012

Krishna, N., & Kumar, P. S. (2016). Impact spallation processes on the Moon: A case study from the size and shape analysis of ejecta boulders and secondary craters of Censorinus crater. *Icarus*, *264*, 274–299. https://doi.org/10.1016/j.icarus.2015.09.033

Krohn, K., Jaumann, R., Elbeshausen, D., Kneissl, T., Schmedemann, N., Wagner, R., et al. (2014). Asymmetric craters on Vesta: Impact on sloping surfaces. *Planetary and Space Science*, *103*, 36–56. https://doi.org/10.1016/j.pss.2014.04.011

Küppers, M., Moissl, R., Vincent, J.-B., Besse, S., Hviid, S. F., Carry, B., et al. (2012). Boulders on Lutetia. *Planetary and Space Science*, *66*, 71–78. https://doi.org/10.1016/j.pss.2011.11.004

Lee, P., Veverka, J., Thomas, P. C., Helfenstein, P., Belton, M. J. S., Chapman, C. R., et al. (1996). Ejecta blocks on 243 Ida and on other asteroids. *Icarus*, *120*(1), 87–105. https://doi.org/10.1006/icar.1996.0039

Lee, S. W., Thomas, P., & Veverka, J. (1986). Phobos, Deimos, and the Moon—Size and distribution of crater ejecta blocks. *Icarus*, *68*, 77–86. https://doi.org/10.1016/0019-1035(86)90075-8

Li, B., Ling, Z., Zhang, J., & Chen, J. (2017). Rock size-frequency distributions analysis at lunar landing sites based on remote sensing and in-situ imagery. *Planetary and Space Science*, *146*, 30–39. https://doi.org/10.1016/j.pss.2017.08.008

Marchi, S., Bottke, W. F., O'Brien, D. P., Schenk, P., Mottola, S., De Sanctis, M. C., et al. (2014). Small crater populations on Vesta. *Planetary and Space Science*, *103*, 96–103. https://doi.org/10.1016/j.pss.2013.05.005

Markwardt, C. B. (2009). Non-linear least-squares fitting in IDL with MPFIT. In D. A. Bohlender, D. Durand, & P. Dowler (Eds.), *Astronomical data analysis software and systems xviii* (Vol. 411, p. 251).

Martin, P. M., & Mills, A. A. (1977). Does the lunar regolith follow rosin's law? *Moon*, *16*(2), 215–219. https://doi.org/10.1007/BF00596726

Mazrouei, S., Daly, M. G., Barnouin, O. S., Ernst, C. M., & DeSouza, I. (2014). Block distributions on Itokawa. *Icarus*, *229*, 181–189. https://doi.org/10.1016/j.icarus.2013.11.010

McCord, T. B., & Gaffey, M. J. (1974). Asteroids: Surface composition from reflection spectroscopy. *Science*, *186*(4161), 352–355. https://doi.org/10.1126/science.186.4161.352

Michikami, T., Honda, C., Miyamoto, H., Hirabayashi, M., Hagermann, A., Irie, T., et al. (2019). Boulder size and shape distributions on asteroid Ryugu. *Icarus*, *331*, 179–191. https://doi.org/10.1016/j.icarus.2019.05.019

Michikami, T., Nakamura, A. M., Hirata, N., Gaskell, R. W., Nakamura, R., Honda, T., et al. (2008). Size-frequency statistics of boulders on global surface of asteroid 25143 Itokawa. *Earth, Planets, and Space*, *60*, 13–20. https://doi.org/10.1186/BF03352757

Molaro, J., & Byrne, S. (2012). Rates of temperature change of airless landscapes and implications for thermal stress weathering. *Journal of Geophysical Research*, *117*, E10011. https://doi.org/10.1029/2012JE004138

Molaro, J. L., Byrne, S., & Le, J.-L. (2017). Thermally induced stresses in boulders on airless body surfaces, and implications for rock breakdown. *Icarus*, *294*, 247–261. https://doi.org/10.1016/j.icarus.2017.03.008

Moore, H. J. (1971). Large blocks around lunar craters. In *Analysis of Apollo 10 photography and visual observations* (pp. 26–27). Washington, DC: NASA SP-232.

Moré, J. J. (1978). The Levenberg-Marquardt algorithm: Implementation and theory. In G. A. Watson (Ed.), *Numerical analysis: Proceedings of the Biennial Conference held at Dundee, June 28–July 1, 1977* (pp. 105–116). Berlin, Heidelberg: Springer. https://doi.org/10.1007/BFb0067700

Nakamura, A. M., Michikami, T., Hirata, N., Fujiwara, A., Nakamura, R., Ishiguro, M., et al. (2008). Impact process of boulders on the surface of asteroid 25143 Itokawa—Fragments from collisional disruption. *Earth, Planets, and Space*, *60*, 7–12. https://doi.org/10.1186/BF03352756

Newman, M. E. J. (2005). Power laws, Pareto distributions and Zipf's law. *Contemporary Physics*, *46*(5), 323–351. https://doi.org/10.1080/00107510500052444

O'Brien, D. P., Marchi, S., Morbidelli, A., Bottke, W. F., Schenk, P. M., Russell, C. T., & Raymond, C. A. (2014). Constraining the cratering chronology of Vesta. *Planetary and Space Science*, *103*, 131–142. https://doi.org/10.1016/j.pss.2014.05.013

O'Brien, D. P., & Sykes, M. V. (2011). The origin and evolution of the asteroid belt—Implications for Vesta and Ceres. *Space Science Reviews*, *163*, 41–61. https://doi.org/10.1007/s11214-011-9808-6

Pajola, M., Oklay, N., La Forgia, F., Giacomini, L., Massironi, M., Bertini, I., et al. (2016). Aswan site on comet 67P/Churyumov-Gerasimenko: Morphology, boulder evolution, and spectrophotometry. *Astronomy & Astrophysics*, *592*, A69. https://doi.org/10.1051/0004-6361/201527865

Pajola, M., Pozzobon, R., Lucchetti, A., Rossato, S., Baratti, E., Galluzzi, V., & Cremonese, G.(2019). Abundance and size-frequency distribution of boulders in Linné crater's ejecta (Moon). *Planetary and Space Science*, *165*, 99–109. https://doi.org/10.1016/j.pss.2018.11.008

Pajola, M., Rossato, S., Baratti, E., Pozzobon, R., Quantin, C., Carter, J., & Thollot, P. (2017). Boulder abundances and size-frequency distributions on Oxia Planum-Mars: Scientific implications for the 2020 ESA ExoMars rover. *Icarus*, *296*, 73–90. https://doi.org/10.1016/j.icarus.2017.05.011

Pajola, M., Vincent, J.-B, Güttler, C., Lee, J.-C., Bertini, I., Massironi, M., et al. (2015). Size-frequency distribution of boulders ≥7 m on comet 67P/Churyumov-Gerasimenko. *Astronomy & Astrophysics*, *583*, A37. https://doi.org/10.1051/0004-6361/201525975

Prettyman, T. H., Mittlefehldt, D. W., Yamashita, N., Lawrence, D. J., Beck, A. W., Feldman, W. C., et al. (2012). Elemental mapping by dawn reveals exogenic H in Vesta's regolith. *Science*, *338*, 242. https://doi.org/10.1126/science.1225354

Reddy, V., Le Corre, L., O'Brien, D. P., Nathues, A., Cloutis, E. A., Durda, D. D., et al. (2012). Delivery of dark material to Vesta via carbonaceous chondritic impacts. *Icarus*, *221*, 544–559. https://doi.org/10.1016/j.icarus.2012.08.011

Roatsch, T. h., Kersten, E., Matz, K. D., Preusker, F., Scholten, F., Elgner, S., et al. (2013). High-resolution Vesta Low Altitude Mapping Orbit Atlas derived from Dawn Framing Camera images. *Planetary and Space Science*, *85*, 293–298. https://doi.org/10.1016/j.pss.2013.06.024

Rosin, P., & Rammler, E. (1933). The laws governing the fineness of powdered coal. *Journal of the Institute of Fuel*, *7*, 29–36.

Ruesch, O., Hiesinger, H., Blewett, D. T., Williams, D. A., Buczkowski, D., Scully, J., et al. (2014). Geologic map of the northern hemisphere of Vesta based on Dawn Framing Camera (FC) images. *Icarus*, *244*, 41–59. https://doi.org/10.1016/j.icarus.2014.01.035

Russell, C. T., Capaccioni, F., Coradini, A., de Sanctis, M. C., Feldman, W. C., Jaumann, R., et al. (2007). Dawn Mission to Vesta and Ceres. Symbiosis between Terrestrial Observations and Robotic Exploration. *Earth Moon and Planets*, *101*, 65–91. https://doi.org/10.1007/s11038-007-9151-9

Russell, C. T., Raymond, C. A., Coradini, A., McSween, H. Y., Zuber, M. T., Nathues, A., et al. (2012). Dawn at Vesta: Testing the protoplanetary paradigm. *Science*, *336*, 684–686. https://doi.org/10.1126/science.1219381

Schmedemann, N., Kneissl, T., Ivanov, B. A., Michael, G. G., Wagner, R. J., Neukum, G., et al. (2014). The cratering record, chronology and surface ages of (4) Vesta in comparison to smaller asteroids and the ages of HED meteorites. *Planetary and Space Science*, *103*, 104–130. https://doi.org/10.1016/j.pss.2014.04.004

Schröder, S. E., Mottola, S., Keller, H. U., Raymond, C. A., & Russell, C. T. (2013). Resolved photometry of Vesta reveals physical properties of crater regolith. *Planetary and Space Science*, *85*, 198–213. https://doi.org/10.1016/j.pss.2013.06.009

Schulzeck, F., Schröder, S. E., Schmedemann, N., Stephan, K., Jaumann, R., Raymond, C. A., & Russell, C. T. (2018). Global and local re-impact and velocity regime of ballistic ejecta of boulder craters on Ceres. *Planetary and Space Science*, *153*, 142–156. https://doi.org/10.1016/j.pss.2018.02.004

Senthil Kumar, P., Sruthi, U., Krishna, N., Lakshmi, K. J. P., Menon, R., Amitabh, et al. (2016). Recent shallow moonquake and impact-triggered boulder falls on the Moon: New insights from the Schrödinger basin. *Journal of Geophysical Research: Planets*, *121*, 147–179. https://doi.org/10.1002/2015JE004850

Shoemaker, E. M., & Morris, E. C. (1968). Size-frequency distribution of fragmental debris, *Surveyor Project Final Report. Part II. Science Results* (pp. 86–102). Pasadena, California: Jet Propulsion Laboratory. Technical Report 32-1265.

Sierks, H., Keller, H. U., Jaumann, R., Michalik, H., Behnke, F., Bubenhagen, F., et al. (2011). The Dawn Framing Camera. *Space Science Reviews*, *163*(1–4), 263–327. https://doi.org/10.1007/s11214-011-9745-4

Thomas, P. C., Veverka, J., Robinson, M. S., & Murchie, S. (2001). Shoemaker crater as the source of most ejecta blocks on the asteroid 433 Eros. *Nature*, *413*, 394–396. https://doi.org/10.1038/35096513

Thomas, P. C., Veverka, J., Sullivan, R., Simonelli, D. P., Malin, M. C., Caplinger, M., et al. (2000). Phobos: Regolith and ejecta blocks investigated with Mars Orbiter Camera images. *Journal of Geophysical Research*, *105*, 15,091–15,106. https://doi.org/10.1029/1999JE001204

Williams, D. A., Denevi, B. W., Mittlefehldt, D. W., Mest, S. C., Schenk, P. M., Yingst, R. A., et al. (2014). The geology of the Marcia quadrangle of asteroid Vesta: Assessing the effects of large, young craters. *Icarus*, *244*, 74–88. https://doi.org/10.1016/j.icarus.2014.01.033

Williams, D. A., Jaumann, R., McSween, H. Y., Marchi, S., Schmedemann, N., Raymond, C. A., & Russell, C. T. (2014). The chronostratigraphy of protoplanet Vesta. *Icarus*, *244*, 158–165. https://doi.org/10.1016/j.icarus.2014.06.027

Wingo, D. R. (1989). The left-truncated Weibull distribution: Theory and computation. *Statistical Papers*, *30*(1), 39–48. https://doi.org/10.1007/BF02924307

Yingst, R. A., Mest, S. C., Berman, D. C., Garry, W. B., Williams, D. A., Buczkowski, D., et al. (2014). Geologic mapping of Vesta. *Planetary and Space Science*, *103*, 2–23. https://doi.org/10.1016/j.pss.2013.12.014